JGR Oceans

RESEARCH ARTICLE
10.1029/2021JC018161

Light Under Arctic Sea Ice in Observations and Earth System Models

Marion Lebrun[1,2], Martin Vancoppenolle[1], Gurvan Madec[1], Marcel Babin[1], Guislain Becu[2], Antonio Lourenço[1], Daiki Nomura[3,4,5], Frederic Vivier[1], and Bruno Delille[6]

[1]Sorbonne Université, LOCEAN-IPSL, CNRS/IRD/MNHN, Paris, France, [2]Takuvik International Research Laboratory, Université Laval and CNRS, Université Laval, Quebec City, QC, Canada, [3]Field Science Center for Northern Biosphere, Hokkaido University, Hakodate, Japan, [4]Faculty of Fisheries Sciences, Hokkaido University, Hakodate, Japan, [5]Arctic Research Center, Hokkaido University, Sapporo, Japan, [6]Unité d'Océanographie Chimique, Université de Liège, Liège, Belgium

Abstract The intensity and spectrum of light under Arctic sea ice, key to the energy budget and primary productivity of the Arctic Ocean, are tedious to observe. Earth System Models (ESMs) are instrumental in understanding the large-scale properties and impacts of under-ice light. To date, however, ESM parameterizations of radiative transfer have been evaluated with a few observations only. From observational programs conducted over the past decade at four locations in the Northern Hemisphere sea ice zone, 349 observational records of under-ice light and coincident environmental characteristics were compiled. This data set was used to evaluate seven ESM parameterizations. Snow depth, melt pond presence and, to some extent, ice thickness explain the observed variance in light intensity, in agreement with previous work. The effects of Chlorophyll-a are also detected, with rather low intensity. The spectral distribution of under-ice light largely differs from typical open ocean spectra but weakly varies among the 349 records except for a weak effect of snow depth on the blue light contribution. Most parameterizations considered reproduce variations in under-ice light intensity. Large errors remain for individual records, on average by a factor of ∼3, however. Skill largely improves if more predictors are considered (snow and ponds in particular). Residual errors are attributed to missing physics in the parametrizations, inconsistencies in the model-observation comparison protocol, and measurement errors. We provide recommendations to improve the representation of light under sea ice in the ice-ocean model NEMO, which may also apply to other ESMs and help improve next-generation ESMs.

Plain Language Summary The Arctic sea ice cover has rapidly decreased over the last four decades, and Earth System Models (ESMs) project a complete decay of summer Arctic sea ice in the coming decades. As a result, phytoplankton, micro-algae growing and drifting within seawater, experience increased light supply, favorable to photosynthesis. Phytoplankton is central to the Arctic marine ecosystem, because of its role as a carbon source to the whole food chain. However, there is low confidence in the capacity of models to project Arctic phytoplankton. This is because of large difficulties in simulating nutrient and light supply mechanisms, stemming from limits in basic understanding. Here we gather and analyze a large database of observations of the sea ice environment from the Northern Hemisphere. Snow depth and melt ponds emerge as key drivers of the under-ice light climate. We also evaluate and improve a calculation method for light intensity and color used in several ESMs, and largely improve agreement with observations as compared with reference. Our results will contribute to lower uncertainties in light climate under sea ice in future ESM projections.

Key Points:

- Snow depth, melt ponds, ice thickness, Chlorophyll-a in sea ice, influence under-ice light intensity and spectral distribution
- Seasonal variations in light intensity under sea ice are reproduced by Earth System Model parameterizations informed by observed environmental conditions
- Large uncertainties stem from measurement errors, missing physics in the parameterizations, and inconsistent comparison protocol

Supporting Information:

Supporting Information may be found in the online version of this article.

Correspondence to:

M. Lebrun,
marion.lebrun@locean.ipsl.fr

Citation:

Lebrun, M., Vancoppenolle, M., Madec, G., Babin, M., Becu, G., Lourenço, A., et al. (2023). Light under Arctic sea ice in observations and Earth System Models. *Journal of Geophysical Research: Oceans*, *128*, e2021JC018161. https://doi.org/10.1029/2021JC018161

Received 26 OCT 2021
Accepted 20 JAN 2023

Author Contributions:

Conceptualization: Marion Lebrun, Martin Vancoppenolle, Gurvan Madec
Data curation: Marion Lebrun, Martin Vancoppenolle, Marcel Babin, Guislain Becu, Antonio Lourenço, Daiki Nomura, Frederic Vivier, Bruno Delille
Formal analysis: Marion Lebrun, Martin Vancoppenolle
Writing – original draft: Marion Lebrun, Martin Vancoppenolle

1. Introduction

The changes in Arctic phytoplankton activity observed in recent decades related to changing Arctic sea ice and ocean conditions (Ardyna & Arrigo, 2020; Arrigo & van Dijken, 2015; Lewis et al., 2020) are expected to continue in this century (SIMIP Community, 2020; Vancoppenolle et al., 2013), with important implications for the Arctic marine food web (Post, 2017). However, large uncertainties remain, mostly due to a lack of knowledge of phytoplankton activity in the subglacial environment, hardly observable from satellites (Ardyna et al., 2020). Earth System Models (ESMs) and their sub-components foster progress in the knowledge of the Arctic Ocean phytoplankton and help quantifying pan-Arctic marine primary production (Clement Kinney et al., 2020; Horvat et al., 2020; Zhang et al., 2015). However, in the Arctic, ESMs inconsistently simulate the factors limiting phytoplankton growth, namely nutrients and light levels (Popova et al., 2012; Vancoppenolle et al., 2013).

Writing – review & editing: Marion Lebrun, Martin Vancoppenolle, Gurvan Madec, Marcel Babin, Guislain Becu, Antonio Lourenço, Daiki Nomura, Frederic Vivier, Bruno Delille

In the Arctic, phytoplankton is exposed to generally low and highly variable light intensity (Ardyna et al., 2020; Hill et al., 2018; Katlein et al., 2019). Solar radiation shows large seasonal variations between polar day and night (Berge et al., 2015; Peixoto & Oort, 1992) and is highly reflected by sea ice (Perovich, 2017). Deep snow and thick ice increase surface albedo and reduce light intensity under sea ice, while openings in sea ice, melt ponds and wet snow reduce albedo and increase transmission (Assmy et al., 2017; Ehn et al., 2011; Grenfell & Maykut, 1977; Katlein et al., 2015; Light et al., 2008). As sea ice conditions are highly variable at the meter scale, under-ice variations in light intensity span several orders of magnitude (Katlein et al., 2015; Matthes et al., 2020) and superimpose on the strong seasonal component (Hill et al., 2018; Katlein et al., 2019). Understanding of light under sea ice remains limited, though, and time series of under-ice light intensity can be difficult to interpret (see e.g., Arndt et al., 2017; Boles et al., 2020).

Some ESMs suggest variations in light intensity under the ice at large space and time scales (Horvat et al., 2017; Stroeve et al., 2021). Yet ESM calculations of under-ice light intensity carry substantial errors due to biased sea ice state or intrinsic parameterization problems (Katlein et al., 2019). This can be expected since the parameterizations of radiative transfer in sea ice were originally designed with the surface energy balance as a target but were never fully evaluated for under-ice light intensity. In addition, ESM parameterizations of radiative transfer in sea ice present important variations (Keen et al., 2021, Table 2). A first generic approach (which bases on the Apparent Optical Properties or AOPs of sea ice) is to combine albedo empirically calculated from surface state, with some representation of light transmission through sea ice, with varying complexity. Indeed, some ESMs assume no penetration of solar radiation into the sea ice, whereas several others allow it, but only for zero snow depth (Maykut & Untersteiner, 1971). More elaborated empirical representations of light transmission through sea ice, accounting for snow depth, sea ice thickness and melt ponds (Grenfell & Maykut, 1977) are implemented into the LIM1D process model (Vancoppenolle & Tedesco, 2017), the ice-ocean mitGCM model (Castellani et al., 2017) and MPI-ESM (Pedersen et al., 2009). A second approach is the two-stream, four-band scheme of Briegleb and Light (2007), based on the Delta-Eddington approximation of the phase function. Snow, ice and water inherent optical properties (IOPs) are specified as a function of prescribed microstructure profiles. This parameterization is used by the many ESMs using the CICE/Icepack sea ice model (Hunke et al., 2022).

Less documented and investigated are assumptions made in the ocean component on the spectral distribution of light at the ocean surface right under sea ice. In the NEMO ocean model (Madec et al., 2022), the spectral distribution of light at the ocean surface is prescribed, without consideration for the presence of sea ice. Yet the light spectrum right under sea ice can vary considerably, associated with changes in snow depth and Chlorophyll-a (*Chl-a*) content of sea ice (Mundy et al., 2007; Nomura et al., 2020; Perovich, 2017; Wongpan et al., 2018, 2020).

Benefitting from advances in optical instrumentation, numerous under-ice light observations were performed in the Arctic Ocean and other boreal marine waters over the last decade (e.g., Arrigo, 2014; Massicotte et al., 2020; Nomura et al., 2020), allowing a highly needed observation-based evaluation of parameterizations of radiative transfer in ESM sea-ice components. With such a goal in mind, specifically seeking to improve the NEMO-SI^3 ice-ocean model (Madec et al., 2022), we question in this work which of the currently used approaches are the most appropriate for ESM under-ice light intensity calculations, at large spatial and temporal scales. A fairly large number of optical and environmental observations (349 records) were compiled from 4 regions of the Northern Hemisphere (2014–2019), and different ESM parameterizations of radiative transfer in sea ice were tested against it. The reference NEMO-SI^3 approach, several evolutions of the AOP-based approach described above, and the two parameterizations from the CICE/IcePack model were retained.

In Section 2, we present our observational compilation and the retained parameterizations. In Section 3, we describe the main features of the observational database and evaluate how the different ESM parametrizations capture observed light intensity and spectral variations. Results are discussed in Section 4 and the conclusions are given in Section 5.

2. Data and Methods

Our main goal is to evaluate against observations how ESMs represent the under-ice light intensity. To characterize the latter, ESMs generally work with downwelling planar irradiance (W/m^2), often integrated over the full solar spectrum (*broadband irradiance* I, 300–2,800 nm), or split into several spectral bands. Observational devices measure irradiance, either broadband or spectrally resolved ($E(\lambda)$, W/m^2/nm).

Table 1
Summary Description of Observational Campaigns and Measurements: Location and Program Name, Ice Type, Year of Sampling, Total Number of Records (Number of Records With Available Chl-a Is Also Given if Different From Total), Ice Thickness (h_i), Snow Depth (h_s), Ice Chl-a Content ($M^{Chl\text{-}a}$), Transmittance (T), As Well As Under-Ice Irradiant Energy Fraction Within Blue (f_B), Green (f_G), Red (f_R) and Non-Visible Wavebands ($f_{no\text{-}vis}$)

Location (Program)	Ice Type	Year(s)	Records (with *Chl-a*)	h_i [m]	h_s [m]	$M^{Chl\text{-}a}$ [mg/m^2]	$T\ 10^{-2}$	f_B [%]	f_G [%]	f_R [%]	$f_{no\text{-}vis}$ [%]
Baffin bay (GreenEdge)	Fast ice	2015	152	1.21 ± 0.07	0.20 ± 0.11	0.4–35.3	0.6 ± 1.8	46 ± 10	46 ± 6	8 ± 6	15 ± 1
		2016	71 (68)	1.28 ± 0.11	0.19 ± 0.14	0.2–8.9	2.3 ± 3.2	43 ± 5	46 ± 3	11 ± 4	15 ± 1
	Drift ice	2016	34 (6)	0.72 ± 0.18	0.02 ± 0.04	0.01–0.3	11.7 ± 6.2	42 ± 4	40 ± 2	18 ± 4	16 ± 2
Chukchi Sea (SUBICE)	Drift ice	2014	79	1.22 ± 0.19	0.06 ± 0.03	6.2–109.9	6.7 ± 7.5	40 ± 5	44 ± 3	16 ± 2	16 ± 2
Svalbard (OPTIMISM)	Fast ice (Stf)	2016	3	0.63 ± 0.08	0.22 ± 0.14	0.3–1.4	0.5 ± 0.3	46 ± 3	40 ± 2	14 ± 6	13 ± 1
	Fast ice (VMf)	2018	6	0.51 ± 0.12	0.11 ± 0.08	0.6–9.0	0.8 ± 1.0	46 ± 4	40 ± 2	14 ± 5	13 ± 1
Saroma (SLOPE)	Fast ice	2019	4	0.49 ± 0.03	0.07 ± 0.01	22.7–37.6	0.3 ± 0.1	16 ± 1	53 ± 1	31 ± 1	8 ± 1

Note. Stf = Storfjorden, VMf = Van Mijen Fjorden.
Mean ± standard deviation is given, except for *chl-a* for which the range is given.

To characterize under-ice light intensity, we use transmittance:

$$T = I^{tr}/I^{0}. \tag{1}$$

I^{tr} and I^{0} are the under-ice and above-ice downwelling planar broadband irradiances, respectively.

To characterize the under-ice light spectrum, we use the same energy fraction diagnostics as defined in NEMO (Madec et al., 2022), namely the spectral-to-visible energy fraction in the red (R, 600–700 nm), green (G, 500–600 nm), and blue (B, 400–500 nm) bands

$$f_{R/G/B} = \int_{R/G/B} E^{\mathrm{tr}}(\lambda)d\lambda \Big/ \int_{400\,\mathrm{nm}}^{700\,\mathrm{nm}} E^{\mathrm{tr}}(\lambda)d\lambda, \tag{2}$$

and the non-visible to broadband energy fraction

$$f_{\mathrm{no-vis}} = 1 - \int_{400\,\mathrm{nm}}^{700\,\mathrm{nm}} E^{\mathrm{tr}}(\lambda)d\lambda / I^{\mathrm{tr}}, \tag{3}$$

Where $E^{\mathrm{tr}}(\lambda)$ is the under-ice spectral irradiance. These three diagnostics and how they respond to changes in the sea ice environment are compared within observational and ESM frameworks. Below we describe the observations and ESM approaches used to estimate transmittance.

2.1. Observational Sources and Measurements

We assembled above- and under-ice optical measurements with sea ice environmental observations, summarized in Table 1, from a series of field campaigns in four regions of the seasonal sea ice zone in the Northern Hemisphere (see map in Figure 1).

2.1.1. Sampling Sites

The Baffin Bay activities took place in 2015 & 2016 under the auspices of the GreenEdge project. These include two landfast sea ice camps, held from April to July 2015/2016 near Qikiqtarjuaq Island, and a cruise onboard *CCGS Amundsen* across the sea ice edge in June–July 2016. GreenEdge involved many other physical and biogeochemical sampling activities (Massicotte et al., 2020; Oziel et al., 2019; Randelhoff et al., 2019).

The SUBICE Chukchi Sea cruise took place in first-year pack ice, in May–June 2014, on the Chukchi Shelf (Arrigo, 2014; Selz et al., 2018). As for the GreenEdge campaigns, several physical and biogeochemical measurements were collected.

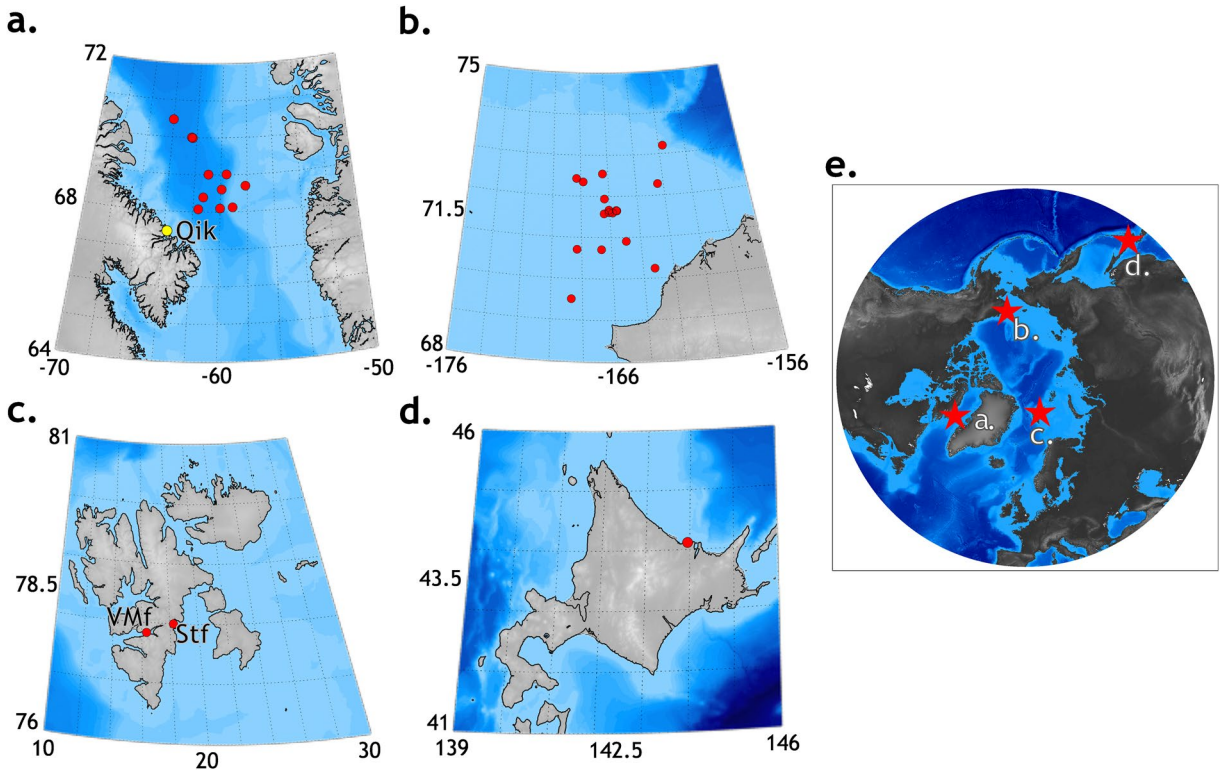

Figure 1. Location of sampling sites (circles) in the 4 different regions: (a) Baffin Bay: red circles = R/V Amundsen cruise stations, yellow circle = Qikiqtarjuaq (Qik) land-fast sea ice site, (b) Chukchi Sea, (c) Svalbard (VMf = Van Mijen Fjorden, Stf = Storfjorden), d, Saroma Lagoon. Red stars in panel e depict the location of each sampling region.

Two other locations were sampled in the framework of smaller-scale activities. The Svalbard activities took place under the auspices of the OPTIMISM-bio project, on landfast sea ice from two different areas (Van Mijenfjorden and Storfjorden), in April, and repeated over 3 years (2016–2018). Nine sampling sessions were completed, three per year of sampling.

Landfast sea ice from the saltwater Saroma-ko Lagoon on the Okhotsk Sea coast of Hokkaido (Japan) was sampled over four days in February 2019 with the same instrument set up as in Svalbard, under the SLOPE project. Other under-ice optical measurements allowed for inter-calibration of our optical instruments with those from other research groups (Nomura et al., 2020).

2.1.2. Snow Depth, Ice Thickness, and Melt Ponds

Snow depth is an average of stick-based measurements; ice thickness is retrieved as the average length of extracted ice cores. At Svalbard and Saroma sites, snow depth and ice thickness were measured within a meter of the light measurement site. At the Baffin Bay and Chukchi Sea sites, they were measured within a few tens of meters of the optical site and may not closely characterize the latter.

As melt ponds are deemed important for the nearby under-ice light field (Frey et al., 2011; Massicotte et al., 2018) and some model parameterizations include the effects of melt ponds, we strived to get an estimate of pond fraction from on-site photography. Pond fraction is set to 5% on the first day of pond appearance, and linearly increases up to 25% at the day of last observation, in line with what is classically seen in the Arctic (Perovich et al., 2002).

2.1.3. *Chl-a* Content From Melted Ice Cores

Chl-a concentration measurements in sea ice are available for 318 of the 349 records. *Chl-a* was measured by fluorometry using standard protocols (Holm-Hansen et al., 1965; Lorenzen, 1967; Yentsch & Menzel, 1963) from melted then filtered ice core sections. In Baffin Bay and Chukchi Sea, only the bottom 10 cm were sampled, whereas in Svalbard and Saroma, full-depth cores were sampled. Volumetric concentrations (in µg/L) were converted into chlorophyll-a content ($M^{Chl\text{-}a}$), that is, vertically-integrated values (mg/m^2, Meiners et al., 2012).

Table 2
Summary Description of the Optical Instruments Relevant to This Study: Two Slightly Differently Configured C-OPS (Compact Optical Profiling System, Biospherical Instruments Inc, Morrow et al., 2010) Radiometer Arrays Used in the GreenEdge and SUBICE Programs; As Well As the Kipp and Zonen CNR4 Pyranometer and the Ocean Optics STS-VIS Micro-Spectrometer (STS) Used in the OPTIMISM and SLOPE Programs

Instrumen	Platform	Spectral channels (range)	Type	Deployment location	Sites
C-OPS	Profiler	19 (320–875 nm)	Irradiance	Above/few cm under ice	Baffin Bay drift ice
		19 (380–875 nm)			Baffin Bay fast ice, Chukchi
CNR4	Tripod	1 (300–2800 nm)	Irradiance	Above ice	Saroma, Svalbard
STS	Profiler	1024 (350–800 nm)	Radiance	0.5–3 m under ice	

As for ice thickness and snow depth, $M^{Chl\text{-}a}$ averages several measurements, made within one m of optical measurements in Svalbard and Saroma, and within a few tens of meters in Baffin Bay and Chukchi Sea. This could affect how well the *Chl-a* values characterize the optical measurements, especially if horizontal variability (patchiness) is high.

2.1.4. Optical Measurements and Processing

Several types of optical measurements above and under sea ice are available. Depending on the case, broadband irradiance, spectral irradiance and seldom spectral radiance (directional) measurements were collected using pyranometers, radiometers and spectrophotometers (see technical specifications in Table 2). Above sea ice, instruments were typically deployed on tripods, whereas under sea ice, they were attached to profiling systems (Nomura et al., 2020; Oziel et al., 2019).

The Baffin Bay and Chukchi sites had C-OPS micro-radiometers (Compact Optical Profiling System, *Biospherical Instruments Inc*, Morrow et al., 2010) measuring irradiance in 19 visible and near-UV channels with 26–29 nm spectral resolution (Oziel et al., 2019), and deployed above and under sea ice. Profilers vertically scanned the upper ∼100 m of the water column under sea ice. Our analysis restricts to measurements performed within 20 cm under sea ice.

At Saroma and Svalbard sites (Nomura et al., 2020), above-ice broadband irradiance was measured with a *Kipp and Zonen* CNR4 pyranometer. Under sea ice, an *Ocean Optics* STS-VIS micro-spectrometer (STS) was deployed on the underwater module of the Ice-T buoy (Vivier et al., 2016), scanning depths between 90 cm and 5 m. The STS measures spectral radiance with a spectral resolution of 10 nm over the 350–800 nm range. Radiance was converted into irradiance assuming an elliptical distribution, an assumption validated from intercalibration with a *TriOS* RAMSES ACC hyper-spectral radiometer deployed nearby on a few occasions during the Saroma campaign (Nomura et al., 2020).

2.1.5. Observation-Based Retrieval of Irradiance, Transmittance and Spectral Energy Fractions

Transmittance and spectral energy fractions were derived from processing optical observations from all instruments at all sites. Raw spectral irradiances were interpolated onto a common 1 nm-resolution grid using a cubic spline method, giving $\tilde{E}(\lambda)$. Above-ice broadband irradiance I^0 was measured directly at Svalbard and Saroma sites. At the Baffin Bay and Chukchi sites I^0 was calculated from above-ice spectral irradiance $\tilde{E}^0(\lambda)$ using $I^0 = 2.1 \times \int_{400\,\mathrm{nm}}^{700\,\mathrm{nm}} \tilde{E}^0(\lambda).d\lambda$, where 2.1 is a visible-to-shortwave conversion factor (Frouin & Pinker, 1995; Stroeve et al., 2021). Under-ice irradiance I^{tr} was obtained by integrating under-ice spectral irradiance $\tilde{E}^{tr}(\lambda)$ over the spectral range of the corresponding instrument. Linear scaling corrections were applied to account for the varying spectral span and deployment depth of under-ice instruments.

Transmittance was obtained from the ratio of above- and under-ice irradiances, see Equation 1. Similarly, spectral energy fractions $f_{\mathrm{no-vis}}$ and $f_{R/G/B}$ were obtained from Equations 2 and 3, using processed spectral irradiance and broadband irradiance data.

Based on an instrument inter-comparison exercise (Nomura et al., 2020), we evaluated observational and sampling errors of 2 W/m^2 for incoming irradiance and 0.1 W/m^2 for transmitted irradiance. Assuming a typical spring-summer value for incoming irradiance (200 W/m^2) and propagating errors in Equation 1, we find the relative error on transmittance is less than 10% for transmittance values $>5 \times 10^{-3}$ (which represents 51% of

Table 3
Transmittance Calculation in the Different Radiative Transfer Parameterizations (See Also Section 2.2.1).

Name	Type	Optically-active components	Tuning	Spectral formulation	Transmittance calculation
NEMO-0	AOP	Ice	No	Broadband	$T_{\text{NEMO-0}} = \begin{cases} i_0(1-\alpha)e^{-k_i(h_i-h_0)} & if\ h_s = 0 \\ 0 & if\ h_s > 0 \end{cases}$
IS	AOP	Ice, snow	Partial	”	$T_{\text{IS}} = \begin{cases} T_{\text{NEMO-0}} & if\ h_s = 0 \\ i_0(1-\alpha)e^{-k_s(h_s-h_0)}e^{-k_i.h_i} & if\ h_s > 0 \end{cases}$
ISP	AOP	Ice, snow, ponds	Full	”	$T_{\text{ISP}} = (1-f_p)T_{IS} + f_p.(1-\alpha_p)\cdot i_{o,p}.e^{-k_i h_i}$
ISPA	AOP	Ice algae	Partial	”	$T_{\text{ISPA}} = T_{\text{ISP}}.e^{-a^*(1+f_{\text{det}})M^{Chl-a}}$
ISdP	AOP	Ice, snow distribution, ponds	Partial	”	$T_{\text{ISdP}} = \int_0^\infty T_{\text{ISP}}(h_s)\cdot g(h_s)\cdot dh_s$
CCSM3	AOP	Patchy snow	No	1 visible + 1 IR	Briegleb et al. (2004)
dEdd	IOP	Ice, snow, ponds	No	1 visible + 3 IR	Briegleb and Light (2007)

Note. The NEMO-0 parameterization originates from the NEMO reference and considers light penetration through bare ice only. IS, ISP, ISPA and ISdP improve over NEMO-0 by considering extra physics in the calculation of vertical light attenuation (S = snow, P = ponds, A = ice Algae, Sd = Snow depth small-scale Distribution). The CCSM3 and dEdd parameterizations are popular options from the CICE/IcePack model (Briegleb and Light, 2007; Briegleb et al., 2004; Hunke et al., 2022). For NEMO-0, CCSM3 and dEdd parameterizations, the tuning parameters (i_o, κ_i, κ_s) were taken from reference publications or code releases; for the IS, ISP, ISdP and ISPA parameterizations, they were tuned against observed transmittance using the ISP parameterization (see Table 4 for values). Independent variables are the ice thickness (h_i), snow depth (h_s), Chl-a content $\left(M^{Chl-a}\right)$ and pond fraction $\left(f_p\right)$. The surface albedo (α) is calculated from h_i and h_s with the parameterization of Shine and Henderson-Sellers (1985). Constant parameters are $\alpha_p = 0.27$ the pond albedo (Lecomte et al., 2015), $i_{o,p} = 0.75$ the surface transmission parameter for ponds, corresponding to 20 cm of water (assumed as mean pond depth), h_o, the surface layer thickness (3 cm for snow and 10 cm for sea ice), $a^* = 0.035\text{m}^{-1}$ per (mg Chl-a / m^3), the specific absorption coefficient of *Chl-a* (Smith et al. 1988), $f^{\text{det}} = 20\%$, an assumed optical contribution of detrital matter. $g(h_s)$ is an idealized snow depth distribution, uniform between zero and twice the mean value. The tuning parameters are i_o the surface transmission coefficient and κ_i and κ_s, the attenuation coefficients for sea ice and snow.

the data set). Above transmittance values of 10^{-3} (75% of the data set), the error is less than 50%. Below 10^{-3}, transmittance retrievals are considered only indicative, as they suffer from large errors, reaching one order of magnitude below 5×10^{-4}.

2.2. Evaluating the ESM Representation of Under-Ice Light Climate

2.2.1. Sea Ice Transmittance Retrieved From ESM Parameterizations of Radiative Transfer

We evaluate several AOP-based parameterizations of shortwave radiation transfer in sea ice designed for ESM use, against observation-based transmittance. Transmittance calculations from the selected ESM parameterizations are summarized in Table 3. More details on the parameterization choices are given hereafter.

Among the selected parameterizations, five use the NEMO (Madec et al., 2022) framework. NEMO calculates irradiance at various depths in the ice based on a specification of sea ice AOPs, as about half of CMIP6 ESMs (see Table 2 in Keen et al., 2021).

Our starting point is the reference parameterization of NEMO (Fichefet & Morales Maqueda, 1997; Maykut & Untersteiner, 1971; Vancoppenolle et al., 2009), referred to as NEMO-0. In this parameterization, snow is considered opaque, only snow-free ice transmits light and other possible contributors (e.g., melt ponds, ice algae) are ignored. Two layers are used to calculate light transmission through bare ice. The uppermost layer is a thin, high scattering layer (*surface scattering layer,* SSL, depth h_o), whereas the lower layer (depth $h - h_o$) is characterized by weak exponential attenuation, following Beer-Bouguer-Lambert law. Therefore, under-ice irradiance reads:

$$I^{tr} = i_o.I^0.(1-\alpha).e^{-\kappa(h-h_o)}. \quad (4)$$

i_o is the surface transmission parameter describing light transmission through the SSL, α is the surface albedo, and κ is the attenuation coefficient (m^{-1}) in the lower ice layer. Reference values for i_o and κ are given in Table 4. Surface albedo is parameterized as a function of environmental conditions, which we further develop later.

Table 4
Values of the Tuning Parameters for the Different AOP-Based Parameterizations

	NEMO-0		IS, ISP, ISPA, ISdP			CCSM3	
	$h_s > 0$	$h_s = 0$	$h_s > 0$		$h_s = 0$	$h_s > 0$	$h_s = 0$
			dry	wet			
i_o	n.a.	0.35–0.53[a]	1	0.45	0.26	n.a.	0.7[d]
h_o (cm)	n.a.	10[a]	0	3[c]	10[a]	n.a.	10[a]
κ_s (m^{-1})	n.a.	n.a.	7	5	n.a.	n.a.	n.a.
κ_i (m^{-1})	n.a.	1[b]	1	1	1	n.a.	1.4[d]

[a]The i_o range reflects variations in cloud fraction (Grenfell and Maykut, 1977). [b]Light et al. (2008). [c]Perovich (2007). [d]Briegleb et al. (2004).

Key drivers of sea ice transmittance, namely snow and melt ponds were identified during analysis. They are missing from the NEMO-0 parameterization and were introduced separately. A first modified parameterization (termed IS) introduces light transmission through snow, using an exponential attenuation approach. In snow, as in other natural media such as seawater or sea ice, exponential attenuation is an imperfect representation of reality. Deviations from exponential behavior would be strongest near the air-snow interface, due to the proximity of a boundary and to rapid changes in IOPs with depth. Deep enough in the medium, however, IOPs are more homogenous, and an asymptotic exponential regime is reached (Mobley, 2022). Single- and two-layer exponential approaches were tested at the tuning stage. The series of experiments aiming at tuning simulated transmittance against observations (see Section 2.2.3) suggests that, in wet snow, best performance is achieved using a two-layer approach, with a thin surface layer ($h_o = 3$ cm, $i_o = 0.45$) and a lower-attenuation layer deeper in the snow ($\kappa_s = 5\ m^{-1}$). By contrast, for dry snow, we found a single-layer approach ($\kappa_s = 7\ m^{-1}$) performs best.

In the ISP parameterization, in addition to snow, melt ponds are considered. Calculated under-ice irradiance is the sum of ponded ice and pond-free ice contributions, weighted by pond fraction. Irradiance under pond-free ice is parameterized exactly as in the IS parameterization. Under ponded ice, irradiance is similarly formulated, but a specific (expectedly larger) surface transmission parameter is used and no SSL is considered. Within an ESM, pond depth could be explicitly considered. Here, as we rely upon pictures to characterize melt ponds, we avoided adding extra uncertainty from ill-known pond depth.

Two extra modifications were added to the ISP parameterization and tested. The first, ISPA, takes ice algae into account. An idealized vertical profile of *Chl-a* is considered by uniformly distributing the observed *Chl-a* content over the bottom 10 cm of the ice and assuming no *Chl-a* elsewhere. We use the value of Smith et al. (1988) for the specific absorption coefficient of ice algae $a^* = 0.035\ m^2/mg$ *Chl-a* and assume that light attenuation increases due to detritus by 20% of the *Chl-a* contribution (Arrigo et al., 1991). The second parameterization, ISdP considers the effect of snow depth variations at small horizontal scales. Transmitted irradiance integrates contributions from the different snow depths, assuming a uniform snow depth distribution between 0 and twice the mean value. The assumption of uniform distribution closely mimics the effect of more complex distributions (e.g., gamma distribution, Abraham et al., 2015).

In order to put the evaluated parameterizations into a broader context, we also consider two widely used CICE/IcePack parameterizations (Hunke et al., 2022). The first one is the 2-band AOP-based, CCSM3 parameterization referred to as CCSM3 (Briegleb et al., 2004). The other (dEdd) is the 3-band, two-stream, IOP-based parameterization of Briegleb and Light (2007), using a Delta-Eddington approximation of the phase function.

2.2.2. Comparison Protocol of Observation- and ESM-Based Sea Ice Transmittance

We compared observation- and ESM-based transmittances as closely as possible. This involves the specification of the relevant environmental characteristics, careful consideration for surface albedo and an appropriate choice of model parameters, which we now describe.

For each observational transmittance value, a corresponding ESM-based value was obtained from each parameterization by applying environmental characteristics from the corresponding sampling location and time. These are observed ice thickness, air temperature and cloud fraction, and, optionally, snow depth, pond fraction and *Chl*-a content. Surface temperature and cloud fraction are required because the state of the surface (melting or not) and the type of light conditions (direct or diffuse light) affect AOPs, namely i_o, κ, *and* α. Surface temperature is well approximated by the near-surface (~1 m) air temperature collected in situ. Cloud fraction is inferred from on-site pictures and/or logbooks and assigned 0 or 1 whether clear or overcast conditions were seen or reported.

For surface albedo, special treatment was applied. The NEMO albedo parameterization is used, rather than observations. This is because much fewer broadband albedo ($N = 32$) than transmittance ($N = 349$) measurements are available in our data set. The NEMO reference albedo parameterization (Shine & Henderson-Sellers, 1985) calculates surface albedo as an empirical function of snow depth, ice thickness, surface temperature and cloud fraction, with pivotal albedo values calibrated from observational studies (Brandt et al., 2005; Grenfell & Perovich, 2004).

This parameterization was tested over the 32 records with measured albedo and environmental parameters. We find the parameterized albedo is biased low, by 0.035 ± 0.07 (see Figure S1 in Supporting Information S1), implying that transmittance is underestimated on average by 3.7×10^{-3} (see Table S1 in Supporting Information S1). Using parameterized rather than observed albedo also allows for the evaluation of the full set of radiative transfer calculations in NEMO, and consistent comparison with CCSM3 and dEdd parameterizations.

The CCSM3 and dEdd parameterizations were taken directly from the original FORTRAN routines (Hunke et al., 2022), and fed with observed snow depth, ice thickness, cloud fraction and air temperature as inputs. We run the calculation routines with 100 W/m^2 as an input for above-ice downwelling irradiance I^0. The corresponding transmittance was obtained by dividing the calculated under-ice irradiance I^{tr} by I^0, and verifiably does not depend on the arbitrary choice of 100 W/m^2 for the I^0 value. The CCSM3 routine includes its own, dual-band albedo parameterization, empirically specifying the albedo as a function of snow depth, ice thickness and surface temperature; whereas in the dEdd routine, albedo is not empirically imposed but diagnostically computed.

2.2.3. Choice and Tuning of Parameters in ESM Parameterizations

Input parameters for all parameterizations are carefully selected (see Table 4). For NEMO-0, CCSM3 and dEdd, we apply the default choices in the published NEMO and CICE/IcePack code references. For the newly developed parameterizations (IS, ISP, ISdP, and ISPA), we rely upon tuning of the ISP parameterization against observed transmittance, retaining surface transmission (i_o) and attenuation (κ) coefficients as free parameters (see Table 4 for final values and Appendix A for details). We assume i_o and κ take specific values for three different surface types: dry snow, wet snow and bare ice. The retained i_o and κ values compromise between low transmittance mean bias and standard deviation of error.

A final remark on parameters: NEMO-0 uses values for the surface transmission parameter (i_o) originally from Grenfell and Maykut (1977), but in a context inconsistent with the original definition. Indeed, Grenfell and Maykut applied i_o to incident solar radiation, whereas here (as in all sea ice models), i_o applies to net solar radiation. Such practice spuriously underestimates transmittance by (1-α) in the NEMO-0 parameterization, but this is not obviously influential here, as our data set has only a few bare ice records. Other parameterizations do not suffer from that issue since i_o is a tuning parameter.

2.2.4. NEMO Assumptions on the Under-Ice Light Spectrum and Their Evaluation

NEMO, as possibly other ocean models, simplifies the spectral distribution of shortwave radiation at the ocean surface without distinguishing between ice-covered and ice-free waters. Downwelling shortwave irradiance right under the ocean surface is divided into one non-visible (near-IR and UV) and three visible (RGB) spectral bands (Lengaigne et al., 2007). The distribution of shortwave energy in the spectral bands is prescribed. A fraction $f_{\text{no-vis}} = 58\%$ of the total (i.e., broadband) energy is assigned to the non-visible band and absorbed in the upper ~50 cm of the ocean. The remainder of the energy (42%) is equally distributed into the three R/G/B bands, that is, $f_{R/G/B} = 1/3$. Energy in these three bands then attenuates with depth in the water using band-specific attenuation coefficients. This approach emulates the 61-band bio-optical model of Morel (1988), itself derived from optical measurements from low and mid-latitude oceans. In order to evaluate the NEMO assumptions on the shortwave energy partitioning in ice-covered waters, $f_{\text{no-vis}}$ and $f_{R/G/B}$ were calculated from optical observations and compared with the default NEMO values.

3. Results

We first describe environmental conditions, in particular the characteristics of the sea ice cover, at the different observation sites. We then focus on the transmittance of the snow-ice system from observations and parameterizations. We finally discuss the spectral distribution of under-ice irradiance and evaluate the corresponding ESM assumptions.

3.1. Environmental Description of the Sites

Observations are exclusively from the Northern Hemisphere. 73% of the records are from Baffin Bay first-year ice, most of which (64% of the total) come from landfast sea ice. 23% of the records document summer first-year pack ice from the Chukchi Sea ice edge region and less than 5% of the records are from Svalbard and Saroma

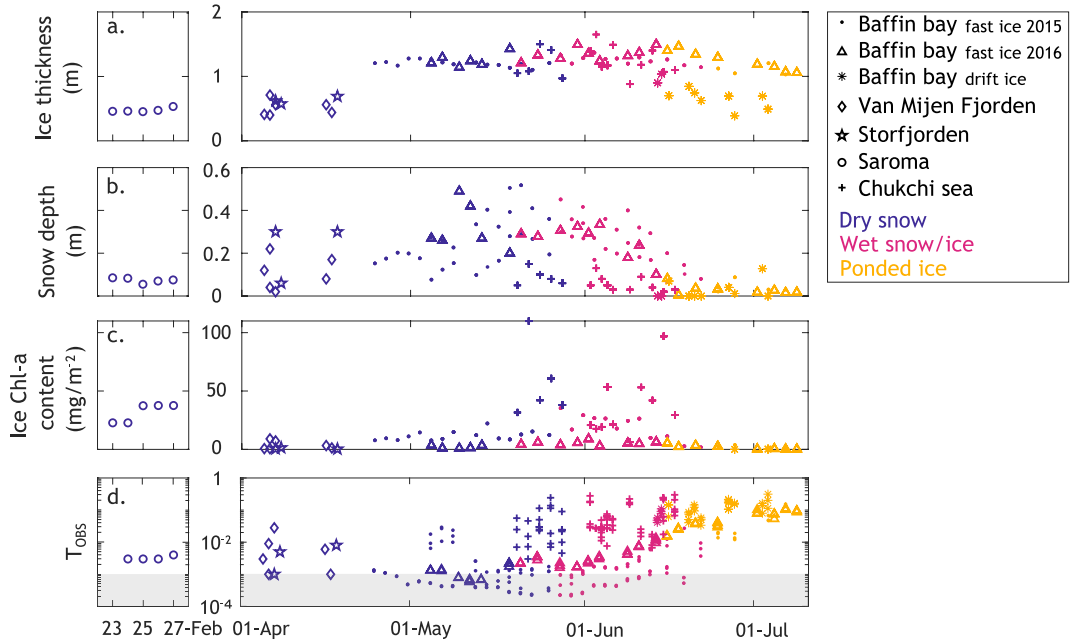

Figure 2. Time series of compiled observations of (a) ice thickness, (b) snow depth, (c) *Chl-a* content in sea ice, and (d) transmittance. Colors highlight three key periods: dry snow, wet snow/ice and melt ponds, whereas symbols refer to the different sampling regions. Gray shading is applied where relative measurement errors on transmittance exceed 50% (see Section 2.1.5).

Lake (see Table 1). Despite a seasonal bias toward spring and early summer, wide-ranging variations in ice thickness (0.4–1.7 m), snow depth (0–0.5 m) and *Chl-a* content in sea ice (0–110 mg/m^2) are covered.

Baffin Bay pack ice, Svalbard and Saroma records come from thin first-year ice (50–70 cm). Records from other regions come from thicker ice (about 120 cm). Snow is generally on the thin end of the range (between 0 and 20 cm), with the highest values in Baffin Bay and Storfjorden landfast sea ice. *Chl-a* content in sea ice ($M^{Chl\text{-}a}$) features large variations in space and time. The lowest $M^{Chl\text{-}a}$ values (<0.1 mg/m^2) are from early spring Baffin Bay pack ice, whereas the largest values (>20 mg/m^2) correspond to the Chukchi Sea and Saroma records. Chukchi Sea records largely differ from the other records in terms of $M^{Chl\text{-}a}$, with much larger and more variable values (44.7 ± 27.3 mg/m^2) than the rest of the data set (11.1 ± 9.6 mg/m^2), and lower snow depth (6 ± 3 cm for Chukchi Sea against 19 ± 14 cm for other records).

Our data set documents the late spring/early summer transition (Figure 2), with a rapid decrease in snow depth, a slow decrease in ice thickness, an overall increase in under-ice irradiance and the development of ice algae over spring and early summer, with highest algal activity from mid-May to mid-June. Several differences can be found between regions. The timing of melt onset and melt ponding onset varies among sites and years of sampling: in 2014, in the Chukchi Sea, the melt season started on June 2; whereas in Baffin Bay, in 2015, melting started on May 25, and in 2016 on May 20. Both Saroma and Svalbard campaigns are too early in the season for surface melting and pond development. Because of late snowfall events and northerly winds during the Chukchi Sea campaign, melt onset occurred later than usual in this region and no melt ponds were reported. In Baffin Bay, melt ponds appeared on June 22 in 2015 and on June 15 in 2016.

During the Chukchi Sea cruise, snow depth seems unimpacted by melt onset. This can be due to the already thin snow at the start of activities or to a sampling artifact. In both 2015 and 2016 Baffin Bay campaigns, snow depth starts decreasing right after melt onset, whereas ice starts thinning shortly after melt ponding onset.

3.2. Under-Ice Irradiance

3.2.1. Physical Drivers of Under-Ice Irradiance

Now we analyze under-ice irradiance and its potential drivers. Observation-based transmittance is log-normally distributed and spans three orders of magnitude (from 2.1 × 10^{-4} to 0.31, median 6.3 × 10^{-3}), with an overall

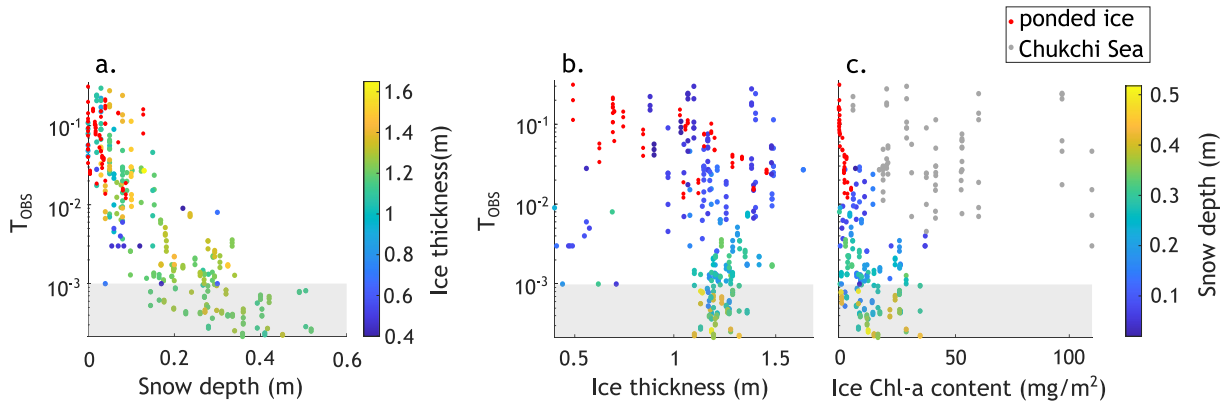

Figure 3. Observed transmittance versus a, snow depth, (b) ice thickness and (c) *Chl-a* content in sea ice. In panel a, color relates to ice thickness, whereas in panels (b and c) color indicates snow depth. In all panels, dots corresponding to reported melt ponds are red. In panel (c) records from the SUBICE campaign (Chukchi Sea), are colored in gray, because they are deemed non-representative of the optical observation sites (see also Section 3.2.1). Gray shading is applied where relative measurement errors on transmittance exceed 50% (see Section 2.1.5).

increase with time of the year. Relationships between the logarithm of transmittance and environmental parameters (snow depth, pond fraction, ice thickness, integrated *Chl-a* content) were analyzed visually (see Figure 3), and quantitatively within a linear regression model framework (Table 5). All *p-values* (p) are much smaller than 0.05.

Snow depth explains the largest fraction of $\log(T)$ variance ($R^2 = 0.73$, see Figure 3a). Pond fraction also explains a significant part of $\log(T)$ variations $\left(R^2 = 0.28\right)$, and a larger part for records with non-zero pond fraction $\left(R^2 = 0.36, N = 65\right)$.

By comparison, variations in ice thickness ($R^2 = 0.09$) and integrated chlorophyll ($R^2 = 0.05$) explain a small fraction of the variance $\log(T)$, when the entire data set is considered. However, restricting the analysis to thin-snow records ($h_s < 5$ cm, N = 84), the strength of the $\log(T)$ — h_i relationship increases $\left(R^2 = 0.31\right)$.

Chukchi Sea (SUBICE) records largely differ from other records in terms of the $\log(T)$ — M^{Chl-a} relationship. For SUBICE records, the latter is weak and insignificant ($R^2 = 0.005$ $p = 0.5, N = 79$). By contrast, when the SUBICE records are excluded ($N = 239$), the $\log(T)$ — M^{Chl-a} relationship is much stronger

Table 5
Summary Statistics of Linear Regression Models, Relating the Observed Optical Diagnostics (Predictands, Columns) to the Sea Ice Environmental Parameters (Predictors, Rows)

		Predictand	log (T)			$f_{no\text{-}vis}$		f_R		f_G		f_B	
Predictor (X)	Subset	#	R^2	p-value	slope	R^2	p-value	R^2	p-value	R^2	p-value	R^2	p-value
Snow depth	All	349	**0.73**	$<10^{-98}$	−5.87	**0.19**	$<10^{-16}$	**0.50**	$<10^{-53}$	**0.090**	$<10^{-7}$	**0.14**	$<10^{-11}$
Ice thickness	All	349	**0.09**	$<10^{-7}$	−1.15	0.001	0.517	**0.14**	$<10^{-12}$	**0.064**	$<10^{-5}$	**0.02**	0.008
Integrated Chl-a	All	318	**0.05**	$<10^{-4}$	0.0092	**0.024**	0.004	0.006	0.1	0.003	0.3	0.0008	0.6
Pond fraction	All	349	**0.28**	$<10^{-25}$	7.49	**0.09**	$<10^{-8}$	**0.17**	$<10^{-14}$	**0.058**	$<10^{-5}$	**0.030**	0.001
Snow depth	$h_s > 1$ cm	326	**0.71**	$<10^{-87}$	−5.81	**0.235**	$<10^{-19}$	**0.49**	$<10^{-48}$	**0.07**	$<10^{-5}$	**0.14**	$<10^{-11}$
Ice thickness	$h_s < 5$ cm	84	**0.31**	$<10^{-8}$	−0.71	0.0003	0.86	**0.19**	$<10^{-4}$	**0.24**	$<10^{-5}$	0.0003	0.9
Integrated Chl-a	no SUBICE	239	**0.27**	$<10^{-17}$	−0.043	**0.048**	$<10^{-3}$	**0.21**	$<10^{-14}$	**0.03**	0.004	**0.05**	$<10^{-3}$
Pond fraction	$f_p > 0$	65	**0.36**	$<10^{-6}$	3.52	0.06	0.04	**0.047**	0.08	**0.23**	$<10^{-4}$	0.05	0.05

Note. Optical diagnostics are the logarithm of transmittance and the under-ice light energy fractions in spectral bands. Models were regressed from the whole observational database (4 uppermost rows) or specific subsets of it (4 lowermost rows). Assuming transmittance T is exponentially related to the environmental variables x, $T = A.e^{(\kappa.x)}$, the logarithm of transmittance is $\log T = \log A + \kappa.x$, hence the slope of the linear regression corresponds to a bulk attenuation coefficient. Bold numbers indicate significant correlations ($p<0.05$).

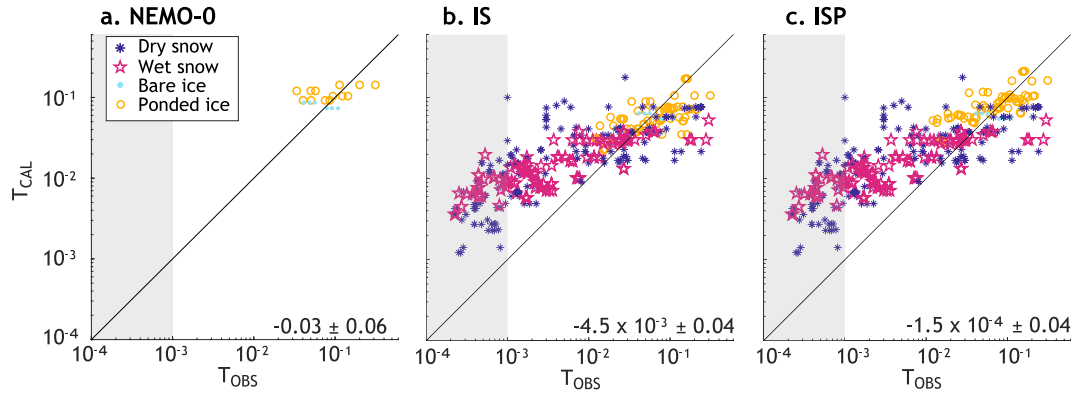

Figure 4. Calculated (T_{CAL}) versus observed (T_{OBS}) transmittance for (a) NEMO-0 (b) IS and (c) ISP parameterizations. NEMO-0 considers ice thickness only, whereas IS adds the effect of snow and ISP the effect of snow and ponds. Colors and symbols highlight different surface types. Because snow transmittance is zero in NEMO-0, records with non-zero snow depth do not appear in panel a. Numbers at the bottom right corner of each panel are calculated minus observed transmittance mean bias error ± standard deviation. Gray shading is applied where relative measurement errors on transmittance exceed 50% (see Section 2.1.5).

($R^2 = 0.27, p < 10^{-17}$, see Figure 3c). In Section 4, we discuss why we consider this is due to high *Chl-a* patchiness and a spatial mismatch between coring and optical sites in our SUBICE data set.

The slope of a linear regression between log(T) and environmental parameters corresponds to a bulk attenuation coefficient (see Table 5 for details). For snow depth, we find bulk attenuation coefficients of 5.81 or 5.87 m^{-1}, whether all records or only those with $h_s > 1$ cm are considered. For ice thickness, we get an attenuation coefficient of 0.71 m^{-1} when considering records with less than 5 cm of snow. When all 349 records are considered, we get a higher value (1.15 m^{-1}). For M^{Chl-a}, we find a rather weakly positive slope of 0.0092 m^2/mg *Chl-a* if all records (i.e., including SUBICE) with available *Chl-a* ($N = 318$) are considered. This would imply an increase in transmittance with *Chl-a* content, opposite to expectation. Without SUBICE records, the slope is negative (−0.043 m^2/mg *Chl-a*), more conform to expectation. Finally, the slope of the relationship between $\log_{10}(T)$ and f_p is 7.5 or 3.5 whether we consider all records or only those with non-zero pond fraction.

The Baffin Bay and Chukchi Sea records are somehow inconsistent in terms of seasonal evolution of transmittance. A rapid increase in transmittance around melt onset is seen in Baffin Bay landfast sea ice records (Figure 2d) associated with an overall reduction in snow depth (Figure 2b) and a change in snow physical properties due to melting. In Chukchi Sea pack ice, however, the transmittance is already in the high range by the second half of May, with no remarkable increase after the detected melt onset, consistent with the stable snow depth after melt onset at this site.

3.2.2. Evaluation of Model Transmittance With Obsermodel Transmittance With Observations

In Figures 4–6 the transmittance calculated from the different radiative transfer parameterizations is plotted against observational values. The NEMO reference parameterization assumes non-zero transmittance only for zero snow depth. Therefore, only the 19 records with zero snow depth have non-zero transmittance and show up in the log-log plot used (see Figure 4). Observations show a quite more nuanced picture than the parameterization with values ranging over 10^{-4} to 10^{-1}. Systematic errors in NEMO-0 lead to a large, negative transmittance bias (MBE ± STD = −0.03 ± 0.06), with the largest amplitude among all evaluated parameterizations.

Considering snow and ponds improves the consistency between calculated and observed transmittance, giving much lower mean bias in the IS parameterization (MBE ± STDE = $-4.5 \times 10^{-3} \pm 4.5 \times 10^{-2}$, Figure 4b) and in ISP ($-1{,}5 \times 10^{-4} \pm 4.3 \times 10^{-2}$, Figure 4c). The ISP statistics are the best we could achieve, since ISP was used for tuning transmittance against observations, in a semi-automated manner (see Section 2.2.3 and Appendix A). However, regardless of the parameterization used and despite tuning, a large dispersion around the $y = x$ line remains (i.e., STDE ∼ 0.04), and more so for transmittance values below 10^{-2}, which correspond to deep snow. The largest systematic errors are also found for deep snow, for which all parameterizations tend to underestimate transmittance by about one order of magnitude.

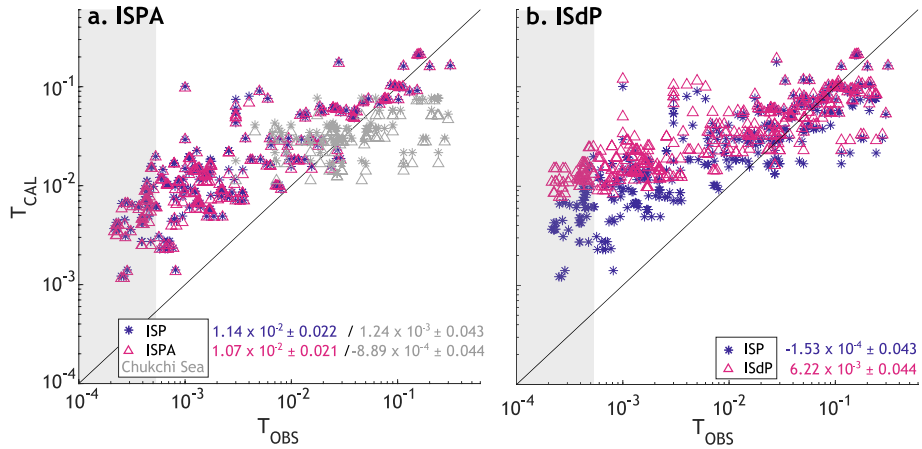

Figure 5. Calculated (T_{CAL}) versus observed (T_{OBS}) transmittance for the ISPA and ISdP parameterizations. ISPA (a) considers the effects of ice algae. ISdP (b) considers the horizontal distribution of snow depth. In both (a, b) results from ISP are given for reference and numbers at the bottom right corner indicate calculated minus observed transmittance (mean bias error ± standard deviation). In panel (a), gray symbols depict Chukchi Sea (SUBICE) records; gray numbers correspond to all records with available *Chl-a* measurements including SUBICE records ($N = 318$), and colored numbers to the same subset but excluding SUBICE records ($N = 239$). In panel (b) numbers are computed with the whole data set ($N = 349$). Gray shading is applied where relative measurement errors on transmittance exceed 50% (see Section 2.1.5).

We now evaluate parameterizations more elaborated than ISP. We first consider the ISPA parameterization, which includes the effects of light absorption by *Chl-a* in sea ice (Figure 5a). Note that only records with a *Chl-a* measurement are retained in this analysis. ISPA gives systematically lower transmittance than ISP, with largest impact for the largest *Chl-a* values. ISPA has measurably better error statistics than ISP, but the differences are small, because records with high *Chl-a* also have low transmittance. The mean transmittance bias to observation is lower in ISPA (-8.9×10^{-4}) than in ISP (1.2×10^{-3}), but STDE is slightly higher in ISPA (4.4×10^{-2}) than in ISP (4.3×10^{-2}). SUBICE records with a weak relationship between *Chl-a* and transmittance could influence the results. Excluding the former, all statistics improve: absolute mean bias is lower in ISPA (1.07×10^{-2}) than in ISP (1.14×10^{-2}); STDE is now also smaller in ISPA (2.11×10^{-2}) than in ISP (2.16×10^{-2}); and the R^2 between observed and calculated transmittance increases, from 0.693 to 0.704.

Second, in the ISdP parameterization, the effects of small-scale snow depth horizontal variations were explored. ISdP calculates the under-ice light intensity with snow depth uniformly distributed from zero and twice the

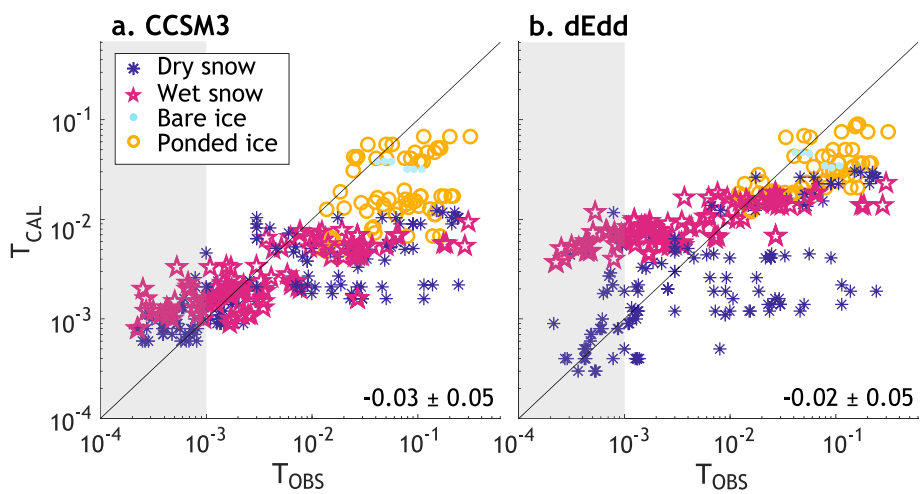

Figure 6. Calculated (T_{CAL}) versus observed (T_{OBS}) transmittance for (a) the CCSM3 parameterization and (b) the 2-stream *Delta-Eddington* method (dEdd). Data is split according to surface type. Calculated minus observed transmittance mean bias error ± standard deviation are given at the bottom right of each panel. Gray shading is applied where relative measurement errors on transmittance exceed 50% (see Section 2.1.5).

Table 6
Performance Statistics from the ISP, CCSM3 and dEdd Parameterizations

	#	ISP (10^{-2})	CCSM3 (10^{-2})	dEdd (10^{-2})
All	349	-0.01 ± 4.3	-2.64 ± 5.3	-2.16 ± 4.9
Dry snow	168	-0.04 ± 4.5	-2.15 ± 5.0	-1.93 ± 4.7
Wet snow	110	-0.001 ± 4.0	-1.32 ± 4.4	-0.70 ± 4.3
Ponded ice	65	0.12 ± 4.6	-6.07 ± 5.9	-5.17 ± 5.4
Bare ice	6	-1.15 ± 3.1	-3.59 ± 3.0	-3.06 ± 3.3
Drift ice	113	-2.48 ± 6.5	-6.82 ± 7.2	-5.91 ± 6.9
Fast ice	236	1.16 ± 1.8	-0.64 ± 2.0	-0.37 ± 1.9
Baffin Bay 2015 (fast)	152	0.91 ± 1.1	-0.36 ± 1.6	-0.05 ± 1.5
Baffin Bay 2016 (fast)	71	0.78 ± 1.0	-1.42 ± 2.6	-1.15 ± 2.4
Baffin Bay 2016 (drift)	34	-1.36 ± 5.7	-8.21 ± 6.6	-6.91 ± 6.2
Chukchi Sea (drift)	79	-2.97 ± 6.8	-6.22 ± 7.4	-5.47 ± 7.2
Van Mijen Fjorden (fast)	6	6.69 ± 5.1	0.04 ± 0.7	0.06 ± 0.5
Storfjorden (fast)	3	3.35 ± 4.5	-0.04 ± 0.5	-0.23 ± 0.5
Saroma (fast)	4	6.14 ± 1.2	0.57 ± 0.13	0.21 ± 0.1

Note. Mean bias error (MBE) ± standard deviation of error (STDE), calculated minus observed. Calculations were performed for several subsets of the observational compilation, splitting according to surface type, ice type, and observation program.

mean. ISdP assumes thin snow is present even when snow is deep on average, which increases the lowest transmittances by up to an order of magnitude. This has a remarkable effect on the mean bias (-1.53×10^{-4} in ISP and 6.22×10^{-3} in ISdP) and reinforces the existing bias toward the overestimation of low transmittance values.

Two other radiative transfer parameterizations used in ESMs (CCSM3 and dEdd) have also been evaluated using the same framework (Figure 6). Both parameterizations were not tuned to the observations like the ISP parameterization (and IS, to a lesser extent). The absence of tuning most likely explains why the bias is $>10^{-2}$ for CCSM3 and dEdd, against $>10^{-4}$ for ISP (Table 6). By contrast, the three parameterizations are much closer in terms of STDE (between 4.3 and 5.3×10^{-2}).

Finally, for all parameterizations, the bias is 2–10 times higher on average and errors are more variable (STDE is 2–3.5 times higher) in pack ice than in landfast ice.

3.3. Spectral Distribution of Downwelling Shortwave Radiation Under Sea Ice

We now evaluate the NEMO assumptions regarding the spectral distribution of downwelling shortwave radiation under sea ice.

First, the fraction of non-visible to total shortwave energy, averaged over all observations, is $f_{\text{no-vis}} = 0.15 \pm 0.016$, which is much lower than 0.58, the reference NEMO value for near-surface ice-free waters (Table 1, Figure 7). Of this non-visible light, ~30% is IR whereas ~70% is ultra-violet (UV), according to Baffin Bay pack ice records, which have the widest wavelength coverage (320–875 nm). There are variations in $f_{\text{no-vis}}$ that can be partly attributed to environmental parameters (see Table 5), mostly due to variations in IR absorption. $f_{\text{no-vis}}$ decreases with snow depth ($R^2 = 0.19$, $p < 10^{-16}$): mean $f_{\text{no-vis}}$ is 0.162 where $h_s \leq 5$ cm and 0.152 for higher snow depth values. More melt ponds increase $f_{no\text{-}vis}$, which is higher under ponded ice (0.163) than with no ponds (0.152). $f_{\text{no-vis}}$ is also larger under overcast skies (0.154) than under clear skies (0.149). All these differences conform to expectation but are small, corresponding to a few tenths of watts per square meter at most.

Second, energy fractions in RGB bands are less even than in open water, with a shift of energy toward blue wavelengths: $f_B = 0.43 \pm 0.08$, $f_G = 0.45 \pm 0.05$ and $f_R = 0.12 \pm 0.07$ (Figures 7a and 7b). Variations around the mean are smaller than the mean, and somehow larger for blue and red than for green bands. Variations in f_R can largely be attributed to snow depth ($R^2 = 0.50$); to a lesser extent to pond fraction ($R^2 = 0.17$) and ice thickness ($R^2 = 0.14$). Ignoring SUBICE records, one finds $M^{Chl\text{-}a}$ also explains a large part of the variability in f_R

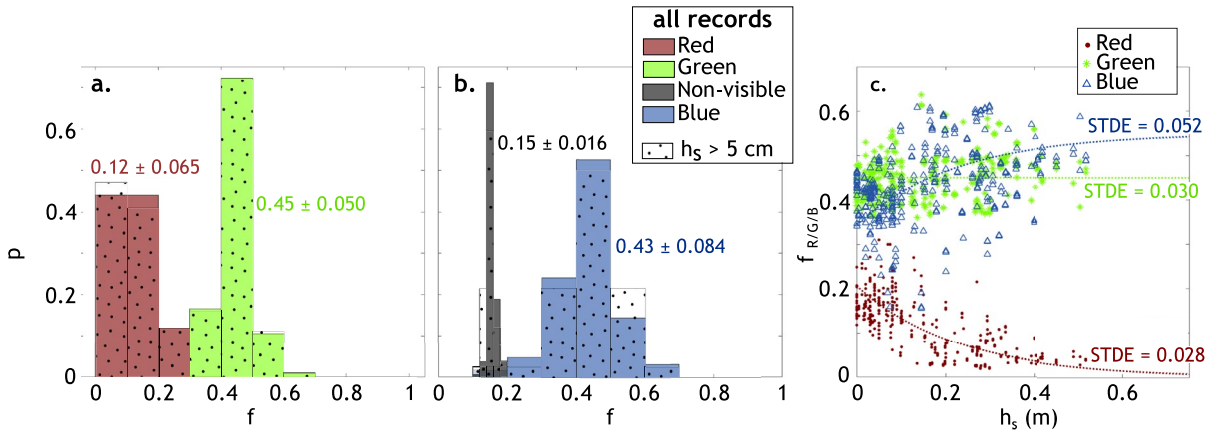

Figure 7. (a, b) Probability histograms of energy fractions in red (f_R), green (f_G) and blue (f_B) bands relative to total visible; and in non-visible band relative to total shortwave ($f_{\text{no-vis}}$, see Section 2 for definitions), for all records (color) and records with snow deeper than 5 cm (dots). Numbers refer to mean ± standard deviation over the whole data set. Bin width is 0.1 for f_R, f_G, and f_B; and 0.02 for $f_{\text{no-vis}}$. (c) f_R, f_G, and f_B versus snow depth from all observational records (dots, stars and triangles), and from the proposed parameterization (Equation 5, dotted lines). Calculated minus observed standard deviation of absolute error (STDE) is given for each waveband along the corresponding curve.

($R^2 = 0.21$). The red fraction decreases with snow depth: $f_R = 0.17$ for records with $h_s \leq 5$ cm and 0.10 otherwise (Figures 7c, Table 5). This is consistent with more absorption at larger wavelengths by snow (Perovich, 1996). Linear regressions between f_B or f_G and environmental parameters are weaker and less significant (Table 5).

The NEMO representation of the spectral distribution of downwelling shortwave irradiance under sea ice, based on constant values derived from open water conditions, can easily be improved. A straightforward approach is to replace the reference values for spectral energy fraction parameters with under-ice mean values, that is, $f_{\text{no-vis}} = 0.15, f_B = 0.43, f_G = 0.45$, and $f_R = 0.12$. A more elaborated approach can reproduce the essential changes in R-G-B fractions in response to snow depth changes (see Figure 7e). Imposing that fractions sum to one, we propose an exponential fit with snow depth for red fraction, a constant value for green fraction, and the residual for blue fraction, giving:

$$\begin{cases} f_R = 0.21e^{(-4.39\,h_s)}, \\ f_G = 0.45, \\ f_B = 1 - f_R - f_G. \end{cases} \tag{5}$$

The exponential fit for snow depth captures more than half of the variance in f_R ($R^2 = 0.504$), which is slightly better than a linear fit ($R^2 = 0.496$). Using Equation 5 reduces the standard deviation of error for RGB fractions: STDE is 0.026 for f_R (instead of 0.034 for constant f_R) and 0.052 for f_B (instead of 0.055). Approaches are identical for f_G, giving STDE = 0.030.

4. Discussion

4.1. Observational Compilation Is Robust and Representative of Arctic Conditions

In this work, several ESM parametrizations of radiative transfer in sea ice were evaluated using a compilation of optical and environmental observations from northern hemisphere sea ice field surveys. We argue that this compilation is robust and representative of Arctic conditions.

Variations in light intensity under the ice in response to environmental changes are consistent with physical expectations and previous work. Mean observed sea ice transmittance of $3.4 \pm 5.8 \times 10^{-2}$ compares with $4.3 \pm 2.2 \times 10^{-2}$ reported by Katlein et al. (2019) from 35,642 Arctic records. Distribution is log-normal, reflecting an exponential dependence on normally-distributed predictors. Three-quarters of variations in the log of transmittance come from snow depth, consistently with Baltic Sea (Arst et al., 2006; Kari et al., 2020) and Arctic

(Anhaus et al., 2021) observations, indicating an important role for snow in the light intensity under the sea ice. Other environmental parameters (melt ponds, ice thickness and *Chl-a* in sea ice) have detectable effects, consistent with previous Arctic work (see e.g., Frey et al., 2011; Katlein et al., 2015; Mundy et al., 2007), but play a role at specific times of the year. That transmittance decreases with snow depth, ice thickness and *Chl-a* content, and increases with melt pond fraction is consistent with state-of-the-art radiative transfer physics (see e.g., Light et al., 2008; Perovich, 1996).

Observation-based bulk attenuation coefficients fall in the literature range. $\kappa_s = 5.9 \pm 0.19$ m^{-1} lies in the lower part of the 3–30 m^{-1} range suggested by Perovich (2007). $\kappa_i = 0.71 \pm 0.12$ m^{-1} is obtained when considering records with less than 5 cm snow, which is consistent with Arctic summer ice values of 0.6 and 0.8 m^{-1}, respectively observed for bare and ponded ice (Light et al., 2008). When all 349 records are considered, we get a higher value (1.15 ± 0.20 m^{-1}), consistent with 1.12 ± 0.19 m^{-1} reported from robust Arctic FY ice recently reported by Veyssière et al. (2022). For *Chl-a* specific attenuation, we get 0.043 ± 0.005 m^2/mg *Chl-a*, leaving SUBICE records aside. For a consistent comparison with the ISPA framework, a 20% contribution of detritus to attenuation must be considered (see Table 4), giving $a^* = 0.036 \pm 0.004$ m^2/mg *Chl-a*, which is consistent with $a^* = 0.035$ m^2/mg *Chl-a* from Smith et al. (1988) but >4 times higher than the value of $a^* = 0.008$ m^2/mg *Chl-a* derived from Arrigo et al. (1991). Finally, our best estimate for the slope of the relationship between $\log_{10}(T)$ and f_p is 3.5, implying a one-order-of-magnitude increase in transmittance between bare ice and 20% melt pond coverage, consistent with Frey et al. (2011). Note that the observation-based attenuation coefficients differ from the values resulting from tuning the ISP parametrization (Table 4). Observation-based values apply to a single-exponential framework, whereas the ISP-tuned values apply to a 2-level exponential framework, with separate treatment of dry and wet surfaces.

The light spectrum under sea ice differs widely from typically observed open water spectra, with less energy in the infrared and red and more energy in the blue and green bands, a trend enhanced under deep snow, which is consistent with previous work (see Perovich, 2017 for a review). Yet, overall variations in the color of light under sea ice are small (typical energy fraction variations in RGB bands are about 10% of the average). We attribute this to similar and mostly thickness-independent spectral variations in the optical properties of snow and ice. For both media, absorption increases with wavelength (Warren, 2019), giving similar spectral variations in albedo and attenuation coefficients (Light et al., 2022; Vérin et al., 2022).

Overall, the light intensity and spectrum observed under sea ice appear reliable and representative of Arctic conditions. However, this does not exclude problems, especially methodological ones. Most notable of these is the inconsistency between transmission and *Chl-a* content in the SUBICE observations selected for this study. Indeed, SUBICE recordings taken alone show a small, insignificant, increase in transmission with *Chl-a* in sea ice. This is unexpected, especially because SUBICE recordings have among the largest *Chl*-a values in our compilation (between 6.2 and 109.9 mg/m^2). By contrast, without SUBICE records, transmittance significantly decreases with *Chl-a* content in sea ice, more consistently with expectation. We surmise the absence of a relationship between transmittance and *Chl-a* content in sea ice relates to the combination, specific to SUBICE, of large horizontal variability of *Chl-a* or *patchiness* (see Figure 7 in Arrigo, 2014; Selz et al., 2018) and relative remoteness of optical and coring sites. Based on this, we left SUBICE records aside when concluding on the links between transmittance and *Chl-a* in sea ice. Other methodological issues are that our pond fraction estimates are indirect, which implies significant uncertainty; and that the spectral range of the spectrometers we used is restricted to wavelengths below 875 nm, which could induce a low bias in $f_{\text{no-vis}}$.

Some relationships present in the data set are not necessarily causal. For instance, transmittance in pack ice samples (range 3×10^{-3} — 0.3) appears an order of magnitude higher than in landfast ice (range 2×10^{-4}–0.15, see Table 1). To explain this, one could speculate on different IOPs between pack ice and fast ice, resulting from intrinsic microstructure differences. However, a simpler explanation is that pack ice in our data set has on average thinner snow and larger pond fraction (5 ± 4 cm, 25%) than fast ice (22 ± 1 cm, 15%). Moreover, snow depth, ice thickness, pond fraction and *Chl-a* are not independent. The fraction of common variance between them proves generally well below 10%. However, for all but SUBICE records, snow depth and *Chl-a* in sea ice share 15% of variance, which should be kept in mind when interpreting the linear regression analysis (Table 5).

Finally, although the environmental conditions sampled capture a variety of conditions encountered under Arctic sea ice, the 349 records may not be fully representative. Our compilation only has first-year ice records. However, Veyssière et al. (2022) obtained 1.24 ± 0.26 m^{-1} as a mean bulk extinction coefficient from 12 Arctic multi-year

ice cores, which is compatible with our overall value, and the lack of multi-year ice cores should not strongly affect our analysis. Antarctic sea ice records are also missing, and therefore the effects of specific processes such as surface flooding (Arndt et al., 2017) are not included; and some seasons, especially late summer, are not well sampled. Overall, this may influence mean transmission and dispersion, but not so much its identified dependencies, although some specific modes of variation may remain unnoticed.

4.2. Evaluation of ESM Parameterizations for Under-Ice Light Calculations

The compilation allows testing of ESM parameterizations of radiative transfer in sea ice in a variety of situations. Specifically, we now examine whether the evaluated ESM parametrizations are suitable for under-ice light intensity calculations and whether we find some parametrization strategies better than others.

Generally, since the attenuation of light in the ocean largely depends on wavelength (Morel, 1988), light under sea ice should have a realistic spectral distribution when transmitted to the ocean component. Coupled, spectrally-resolved parameterizations of radiative transfer in both sea ice (e.g., Briegleb & Light, 2007; Jin et al., 2022) and ocean components would achieve this, provided they perform well. In NEMO, however, shortwave radiation is represented as broadband in the sea ice component, and with a few spectral bands in the ocean component. Also, the surface ocean only receives a single field for shortwave radiation intensity. Therefore, assumptions on the spectral distribution of surface shortwave energy must be made. Observations suggest that prescribing the energy fractions in the spectral bands within the oceanic component is appropriate to represent the spectral distribution of light under sea ice. Yet the values of prescribed energy fractions applied under sea ice should differ from those applied in open water conditions. Mainly, instead of 58% of non-visible light (mainly IR, absorbed over a few tens of a cm in the near-surface ocean; Lengaigne et al., 2007; Madec et al., 2022), 15% should be applied below the sea ice. NEMO and perhaps other ocean models fail at this task, which overestimates solar absorption in the near-surface ocean and presumably sea ice melt. Unequal fractions in the RGB bands with more energy in the green and blue bands than in the red bands are also desirable and making them dependent on snow depth (Equation 5) is the most realistic option available.

Regarding the representation of variations in under-ice light intensity, we find that parameterizations considering snow depth, ice thickness and melt pond fraction (ISP, ISPA, ISdP, CCSM3, dEdd) qualitatively reproduce observed transmittance, whereas simpler parameterizations (NEMO-0, IS) miss important seasonal transitions associated with snow or ponds. This is overall consistent with the idea that snow depth, ice thickness and melt pond fraction are well-understood and important drivers of under-ice light intensity.

Using more sophisticated physics (ISPA, ISdP parameterizations) generally does not remarkably improve performance, but this does not mean they are negligible. Indeed, considering the attenuation of light by *Chl-a* in sea ice (ISPA parameterization) reduces the global bias for the transmittance and improves its variability, especially for low values. This could improve the transmission simulated by ESMs in regions of high *Chl-a* and thin snow, such as the Canadian Archipelago or the Antarctic fast ice zone. However, the overall impact may be small, since considering *Chl-a* in ISPA has a small impact on the average transmission error and dispersion over the entire compilation. In addition, accounting for the effect of small-scale variations in snow depth assuming a uniform distribution of snow depth (ISdP parameterization) represents the effect of low snow depths and increases the lowest transmittance values. This reinforces a pre-existent high bias, and therefore deteriorates the transmittance error statistics, which could be because the real distribution of snow depth was not uniform (which can be expected under fast ice, however, there are no observations to confirm or infirm this).

Finally, considering a more elaborated physical framework (CCSM3 and dEdd parameterizations) leads to no improvement. CCSM3 (Briegleb et al., 2004) uses separate bands for visible and infrared radiation in an exponential framework, whereas dEdd (Briegleb & Light, 2007) uses a 4-band, 2-stream framework and a delta-Eddington approximation (Joseph et al., 1976) for radiative transfer. For both parameterizations, the transmittance bias increases, whereas error dispersion (STDE) remains similar, as compared with the ISP parameterization. It would be tempting to conclude that CCSM3 or dEdd are not as good parameterizations as ISP. However, CCSM3 or dEdd were included to test the influence of more elaborate physics but not tuned, as ISP was. If CCSM3 and dEdd had been tuned, the average transmittance bias could have been adjusted to much lower values. That error dispersion (STDE) is similar among ISP, CCSM3 and dEdd parameterizations argues for roughly similar performance among the three schemes and suggests remaining errors are to find elsewhere.

Large residual transmittance errors remain, though. Residual errors are manifested by the large dispersion in the calculated versus observed transmittance plots (e.g., Figures 3–5). Our tuning experience of the ISP parameterization shows that residual errors can be largely reduced but not eliminated. Large post-tuning errors, averaging a factor of about 3, remain. An illustration of the robustness of such errors is that STDE has a non-zero minimum in the explored parameter space, around 4.3×10^{-2} (Figure A1).

Observation errors contribute but are not the only source of residual transmittance errors. The lowest transmittance values, below 10^{-3}, suffer from observation errors above 50%, however above that value, observation errors are smaller than the residual transmittance errors (see Section 2.1.5). Environmental variables used in transmission calculations (ice thickness, snow depth, pond fraction, air temperature) could also suffer from measurement errors. In addition, we use calculated, not observed, surface albedo. In Table S1 in Supporting Information S1, we impose standard perturbations on the environmental variables and assess the impact on the calculated transmittance. We find they sum to 1.3×10^{-2}. Therefore, the errors in the environmental variables are smaller than the overall uncertainty in calculated transmittance (4×10^{-2}) but could contribute to it.

Remaining plausible error sources relate to the model-observation comparison protocol, or missing physics in the parameterizations. Model-observation comparison protocol issues include for instance three-dimensional features in the environment or in the light field (Katlein et al., 2021), which are not, or wrongly, represented in the 1D model framework. For instance, pond fraction is considered, however, the light field also depends on melt pond distribution and geometry (Horvat et al., 2020). Possibly missing physics include the microstructure of snow (crystal size, specific surface area, see Warren, 1982, 2019) and ice (brine and gas inclusions, see Jin et al., 2022; Light et al., 2004; Warren, 2019; Yu et al., 2022). Snow-related issues may seem important, as the largest relative errors coincide with snow-covered ice. Light-absorbing impurities such as black carbon or sediments are also neglected and probably contribute (Goldenson et al., 2012; Light et al., 1998).

4.3. Implications on the Skill of ESMs to Simulate Under-Ice Light Characteristics

What can we tell of the ability of ESMs (or of their sub-components) to simulate under-ice light intensity? Ice-ocean models used to study phytoplankton dynamics over the recent past (Clement Kinney et al., 2020; Gao et al., 2022; Horvat et al., 2017; Zhang et al., 2015) typically consider the effects of snow, ice and melt ponds, and should therefore properly resolve the seasonal evolution of under-ice light. By contrast, the many ESMs with no or oversimplified parameterizations of radiative transfer through sea ice (Keen et al., 2021; Table 2) miss key transitions in the seasonal variations in under-ice light intensity, as we expect for NEMO and as was highlighted due to the lack of consideration for melt ponds in mitGCM (Katlein et al., 2019).

Quantitatively speaking, ESMs may suffer from large errors, including those with the most elaborate radiative transfer parameterizations, since even the latter feature large residual errors. Also, many ESMs probably make wrong assumptions about the spectral distribution of light under sea ice. Furthermore, the simulated under-ice light intensity would be quite sensitive to biases in sea ice state. In most ice-ocean model simulations, such biases are reasonable but not zero (Zhang et al., 2015) and in ESMs, they are commonly quite large (Keen et al., 2021; Roach et al., 2020; SIMIP Community, 2020). In this context, careful examination (and possibly tuning) of simulated under-ice light levels or transmittance would be required to ensure sensible simulations. Specific ESM experiments may also help to understand, quantify and evaluate the impacts of such errors, and the benefits of reducing them. Indeed, impacts on the ocean temperature profile, sea ice mass balance, and phytoplankton phenology remain difficult to assess.

5. Conclusion

Light under the sea ice is a key uncertainty factor in ESM calculations of present and future Arctic marine primary production. To address this issue, we evaluated several contemporary ESM parametrization approaches in their ability to represent light intensity under sea ice. This was accomplished using a compilation of optical observations under (mostly) Arctic sea ice, unique in terms of number of records and availability of environmental metadata.

We find that ESMs are a priori able to simulate the intensity of light under sea ice, provided that the effects of the snow depth, ice thickness, melt ponds and ice algae, are considered in the calculations of radiative transfer in sea ice. The spectral distribution of light under sea ice is also important and must be carefully considered.

Many contemporary ESM sea ice-ocean components do not satisfy the requirements listed above. Moreover, even the most realistic and best tuned ESM parameterizations would imply large errors in simulated under-ice light. Intrinsic errors remain in all parameterizations, stemming from missing, uncertain, or misrepresented physical processes, for instance related to snow and ice microstructure or to the presence in the ice of organic and mineral particles. Improper treatment of small-scale variability in the sea ice medium and in the light field could also largely contribute to uncertainty as already pointed out (Horvat et al., 2020; Katlein et al., 2021).

On this basis, we confirm that light intensity under sea ice as calculated by ESMs may suffer from important errors. To progress, minor modifications of the ESMs along the lines developed in this paper could largely reduce uncertainties in under-ice light climate for the next generation of climate projections. Direct evaluation and possibly tuning of simulated under-ice light in ESMs would help and benefit from including under-ice light intensity and sea ice transmittance as standard ESM outputs (Notz et al., 2016). In the long-term, both experimental and theoretical research on optics in ice-covered seas is needed to fundamentally improve ESM representations.

Appendix A: Tuning the ISP Parameterization of Radiative Transfer in Sea Ice

Improved parameterizations are tuned to observed transmittance statistics, by adjusting three parameters in the reference ISP parameterization: the surface transmission parameter (i_o) and the sea ice and snow attenuation coefficients (κ_i, κ_s, [m^{-1}]). All these take a priori specific values for bare ice, dry snow and wet snow cases, except κ_s, which is undefined over bare ice. The surface albedo, calculated with the modified parameterization of Shine and

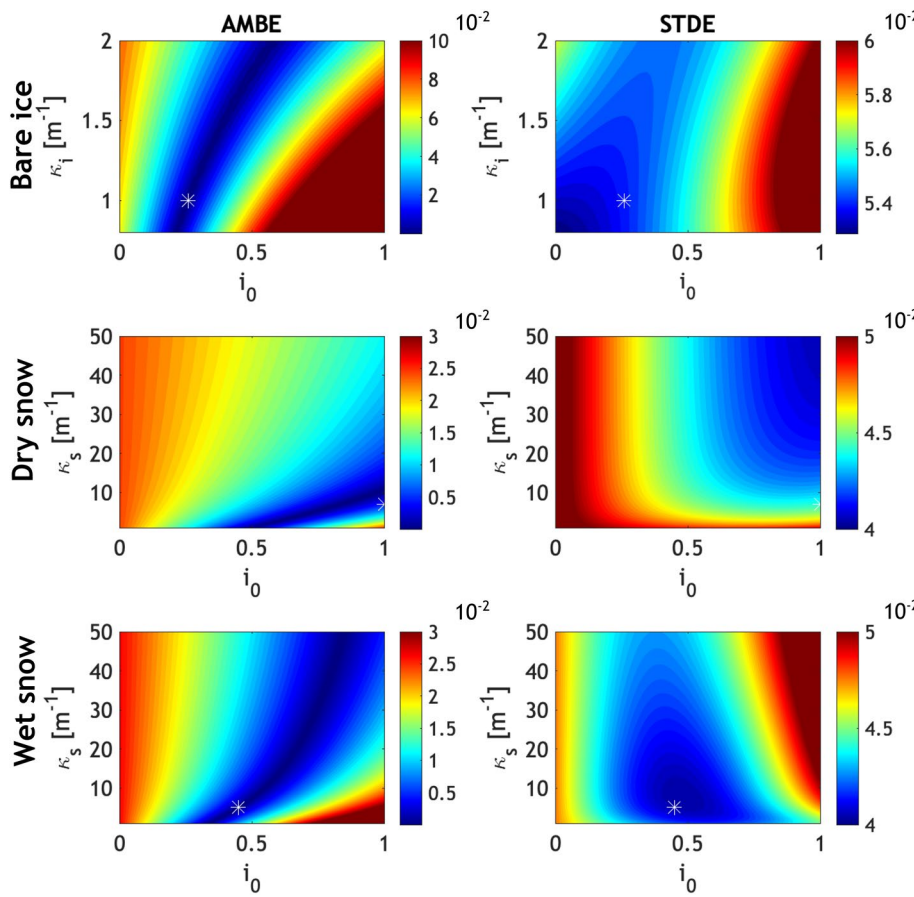

Figure A1. Contour plots of transmittance statistics as a function of model tuning parameters, used to decide the final retained parameter values. Absolute mean bias error (AMBE, left) and standard deviation of error (STDE, right) of transmittance (10^{-2}) as a function of i_o and κ_i for bare ice records (top, $N = 19$) and as a function of i_o and κ_s for dry snow (middle, $N = 169$) and wet snow (bottom, $N = 162$) records. White stars represent the best choice of both parameters to minimize AMBE and STDE.

Henderson-Sellers (1985) is excluded from tuning, because of the relatively low uncertainties on this parameter. We also exclude the SSL thickness parameter h_0, which has a weak influence on retrieved transmittance (changing by about 5% for a 10% change in h_0). h_o is, first, assumed 3 cm for snow-covered ice (Perovich, 2007) and 10 cm for bare ice (Grenfell & Maykut, 1977).

The transmittance statistics retained for optimization are the absolute mean bias error (AMBE) and standard deviation of error (STDE):

$$\mathrm{AMBE}(p_1, p_2) = \left| \frac{1}{N} \sum_{j=1}^{N} \left(T^j_{\mathrm{calc}}(p_1, p_2) - T^j_{\mathrm{obs}} \right) \right|, \tag{A1}$$

$$\mathrm{STDE}(p_1, p_2) = \mathrm{standard\_deviation}\left(T^j_{\mathrm{calc}}(p_1, p_2) - T^j_{\mathrm{obs}} \right), \tag{A2}$$

given a series of selected observational sites (j = *1, …, N*), and a pair of tuning parameters (p_1, p_2). T^j_{obs} is the observational estimate of transmittance at jth site, and $T^j_{\mathrm{calc}}(p_1, p_2)$ the calculated transmittance. Parameters are tuned separately for each surface type (bare ice, dry snow, wet snow).

Tuning is done through the examination of AMBE and STDE contours in two-dimensional parameter space, shown in Figure A1, for the bare ice, dry snow and wet snow sites. The resulting optimized values are given in Table 3. For all surface types, AMBE takes minimum values on a line in 2D parameter space, leaving large freedom on the possible parameter values. STDE provides a stricter constraint, more influential on the final parameter values. STDE typically takes a minimum around 4%, regardless of surface type. The combined minimum AMBE and STDE criteria always provides a single parameter couple.

The range of tested parameter values is selected based on the observational constraints we are aware of Grenfell & Maykut (1977), Järvinen and Leppäranta (2011), Light et al. (2008), Perovich (1996). For i_o, we explore the [0, 1] range with 10^{-2} precision; for κ_i, [0.8, 2 m^{-1}] with a precision of 0.1 m^{-1}; for κ_s, [1, 50 m^{-1}] with 0.1 m^{-1} precision.

Bare ice parameters (i_o and κ_i) are adjusted by fitting the calculated transmittance

$$T^j_{\mathrm{calc}}(i_o, \kappa_i) = i_o \left(1 - \alpha^j\right) . e^{-\kappa_i h^j_i - h_o} \tag{A3}$$

to their observational counterparts T^j_{obs} at the 19 sites with snow depth equal to 0. Observed ice thickness h^j_i, calculated albedo α^j at station j, and h_o = 10 cm are imposed throughout. Optimization leads to i_o = 0.26 and κ_i = 1 m^{-1}, rather close to standard sea ice model values (i_o = 0.17 and κ_i = 1.5 m^{-1}, Maykut & Untersteiner, 1971). As κ_i is barely influential when the ice is snow-covered, we assume κ_i independent of surface type.

Optimal i_0 and κ_s for snow-covered records greatly differ whether snow is dry or wet, which is why we tune dry and wet snow parameters separately. We optimize the following transmittance

$$T^j_{\mathrm{calc}}(i_o, \kappa_s) = i_o \left(1 - \alpha^j\right) . e^{-\kappa_s h^j_s - h_o} . e^{-\kappa_i h^j_i} \tag{A4}$$

at 168 dry snow sites and 110 wet snow sites. Observed snow depth h^j_s, ice thickness h^j_i and calculated albedo α^j at station j, h_o = 3 cm and κ_i = 1 m^{-1} are first imposed. Optimization leads to i_o = 0.45 and κ_s = 5 m^{-1} for wet snow. For dry snow, optimization leads to i_o = 1 whatever the chosen κ_s. The optimal surface transmission is 100% in dry snow hence we consider only one layer in dry snow (h_o = 0; i_o = 1) and only tune κ_s (Figure A2), leading to κ_s = 7 m^{-1}. Both dry and wet snow attenuation coefficients are in the range of observational values, which is rather large (Järvinen & Leppäranta, 2011; Perovich, 2007).

Melt ponds are present for 52 wet snow records and 13 bare ice records. For these records, the calculated transmittance, estimated from either A3 (bare ice records) or A4 (wet snow records), is recombined with an estimation of melt ponds contribution:

$$T^j_{\mathrm{calc}} = f_p T^j_p + (1 - f_p) T^j_{\mathrm{calc}}, \tag{A5}$$

Acknowledgments
We thank all the scientists involved in the SLOPE 2019 campaign for their warm welcome at Saroma-ko lagoon as well as for their contribution to the data collection and processing. We thank all contributors to the GreenEdge project fieldwork, data collection, data provision and support, Marie-Hélène Forget, Joannie Ferland, Flavienne Bruyant, Simon Lambert-Girard, Philippe Massicotte, Christian Haas and the Amundsen Science Data team. We also thank SUBICE contributors for fieldwork and data collection, in particular Gert van Dijken and Donald Perovich. We also thank both anonymous reviewers as well as Camille Lique, Roland Séférian and David Salas y Mélia for their precious comments. M.L. was supported by a CNES (Centre National d'Etudes Spatiales) Postdoctoral Fellowship. This work was supported by the Japan Society for the Promotion of Science (17H04715, 18H03745, 18KK0292, and 20H04345). This paper is a contribution to the SCOR Working Group 152–Measuring Essential Climate Variables in Sea Ice (ECV-Ice) and Biogeochemical Exchange Processes at Sea-Ice Interfaces (BEPSII). The GreenEdge project is funded by the following French and Canadian programs and agencies: ANR (Contract #111112), ArcticNet, CERC on Remote sensing of Canada's new Arctic frontier, CNES (project #131425), French Arctic Initiative, Fondation Total, CSA, LEFE, and IPEV (project #1164). The GreenEdge project would not have been possible without the support of the Hamlet of Qikiqtarjuaq and the members of the community as well as the Inuksuit School and its Principal, Jacqueline Arsenault. The GreenEdge project was conducted under the scientific coordination of the Canada Excellence Research Chair on Remote sensing of Canada's new Arctic frontier, the CNRS & Université Laval Takuvik Joint International Laboratory (UMI3376). It was also conducted using the Canadian research icebreaker CCGS Amundsen with the support of the Amundsen Science program funded by the Canada Foundation for Innovation (CFI) Major Science Initiatives (MSI) Fund. We wish to thank officers and crew of CCGS Amundsen. The field campaign was successful thanks to the contribution of C. Aubry, G. Bécu, M. Benoît-Gagné, F. Bruyant, D. Christiansen-Stowe, E. Devred, J. Ferland, M.-H. Forget, J. Lagunas, C. Lalande, S. Lambert-Girard, J. Larivière, A. LeBaron, C. Marty, E. Rehm, J. Sansoulet, A. Wells from Takuvik laboratory, J. Bourdon, C. Marec and M. Picheral from CNRS, C.J. Mundy and V. Galindo from University of Manitoba & F. Pinczon du Sel and E. Brossier from Vagabond. Michel Gosselin, Québec-Océan, the CCGS *Amundsen* and the Polar Continental Shelf Program have also contributed in terms of polar logistics

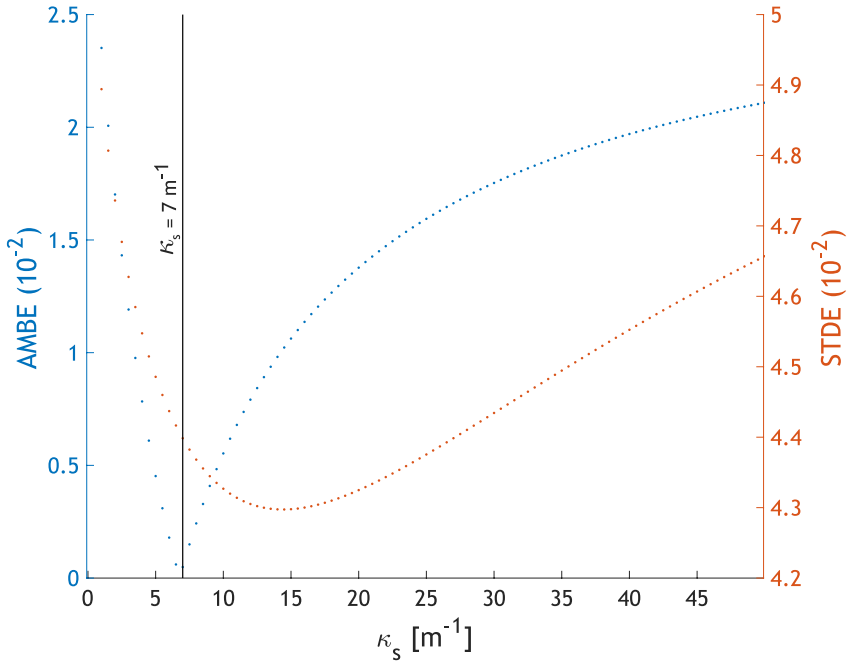

Figure A2. Absolute mean bias error (AMBE, blue) and standard deviation of error (STDE, red) of transmittance (10^{-2}) as a function of κ_s (m^{-1}) for dry snow ($N = 168$) records, considering no surface scattering layer ($i_o = 1$; $h_o = 0$ m and $\kappa_i = 1$ m^{-1}). The black line represents the best choice of κ_s to minimize AMBE and which gives a reasonable STDE.

where f_p is the reconstructed pond fraction (see main text), and T_p^j is the estimated ponded ice transmittance:

$$T_p^j = (1 - \alpha_p).i_{o,p}.e^{-\kappa_i h_i^j}, \tag{A6}$$

where $\alpha_p = 0.27$ is ponded ice albedo and $i_{o,p} = 0.75$ is the transmission parameter of liquid water. We decide not to tune optical parameters for ponded ice, because we have little information on their characteristics.

Conflict of Interest

The authors declare no conflicts of interest relevant to this study.

Data Availability Statement

Raw GreenEdge data are accessible on the SEANOE database (https://doi.org/10.17882/59892). Raw SUBICE data are accessible on the Stanford university database (http://ocean.stanford.edu/subice/) upon request from Gert van Dijken (gertvd@stanford.edu). Scripts and processed data performed in the context of this study are available at zenodo (https://doi.org/10.5281/zenodo.7310958).

References

Abraham, C., Steiner, N., Monahan, A., & Michel, C. (2015). Effects of subgrid-scale snow thickness variability on radiative transfer in sea ice. *Journal of Geophysical Research: Oceans*, 5597–5614. https://doi.org/10.1002/2015JC010741@10.1002/(ISSN)2169-9291

Anhaus, P., Katlein, C., Nicolaus, M., Arndt, S., Jutila, A., & Haas, C. (2021). Snow depth retrieval on arctic sea ice using under-ice hyperspectral radiation measurements. *Frontiers of Earth Science*, *9*. https://doi.org/10.3389/feart.2021.711306

Ardyna, M., & Arrigo, K. R. (2020). Phytoplankton dynamics in a changing Arctic Ocean. *Nature Climate Change*, *10*(10), 892–903. https://doi.org/10.1038/s41558-020-0905-y

Ardyna, M., Mundy, C. J., Mayot, N., Matthes, L. C., Oziel, L., Horvat, C., et al. (2020). Under-ice phytoplankton blooms: Shedding light on the "invisible" part of Arctic primary production. *Frontiers in Marine Science*, *7*. https://doi.org/10.3389/fmars.2020.608032

Arndt, S., Meiners, K. M., Ricker, R., Krumpen, T., Katlein, C., & Nicolaus, M. (2017). Influence of snow depth and surface flooding on light transmission through Antarctic pack ice. *Journal of Geophysical Research: Oceans*, *122*(3), 2108–2119. https://doi.org/10.1002/2016JC012325

Arrigo, K. (2014). *SUBICE—"Study of under-ice blooms in the Chukchi ecosystem", cruise report from HLY1401*. Stanford University. Retrieved from http://icefloe.net/docs/hly1401_cruise_report.pdf

and scientific equipment. The SUBICE project was supported by the NSF Office of Polar Programs (PLR-1304563). The OPTIMISM-bio project was supported by the French Polar Institute (IPEV program 1015) and CNRS (MI). Stefano Poli, Marie Kotovitch and Fanny Vanderlinden are gratefully acknowledged. Funding support from the European Union's Horizon 2020 research and innovation programme under grant agreement No 824084 (IS-ENES3) is acknowledged.

Arrigo, K. R., Sullivan, C. W., & Kremer, J. N. (1991). A bio-optical model of Antarctic sea ice. *Journal of Geophysical Research*, *96*(C6), 10581–10592. https://doi.org/10.1029/91JC00455

Arrigo, K. R., & van Dijken, G. L. (2015). Continued increases in Arctic Ocean primary production. *Progress in Oceanography*, *136*, 60–70. https://doi.org/10.1016/j.pocean.2015.05.002

Arst, H., Erm, A., Leppäranta, M., & Reinart, A. (2006). Radiative characteristics of ice-covered fresh- and brackish-water bodies. *Proceedings of the Estonian Academy of Sciences: Geology*, *55*(1), 3. https://doi.org/10.3176/geol.2006.1.01

Assmy, P., Fernández-Méndez, M., Duarte, P., Meyer, A., Randelhoff, A., Mundy, C. J., et al. (2017). Leads in Arctic pack ice enable early phytoplankton blooms below snow-covered sea ice. *Scientific Reports*, *7*(1), srep40850. https://doi.org/10.1038/srep40850

Berge, J., Renaud, P. E., Darnis, G., Cottier, F., Last, K., Gabrielsen, T. M., et al. (2015). In the dark: A review of ecosystem processes during the Arctic polar night. *Progress in Oceanography*, *139*, 258–271. https://doi.org/10.1016/j.pocean.2015.08.005

Boles, E., Provost, C., Garçon, V., Bertosio, C., Athanase, M., Koenig, Z., & Sennéchael, N. (2020). Under-ice phytoplankton blooms in the central Arctic Ocean: Insights from the first biogeochemical IAOOS platform drift in 2017. *Journal of Geophysical Research: Oceans*, *125*(3), e2019JC015608. https://doi.org/10.1029/2019JC015608

Brandt, R. E., Warren, S. G., Worby, A. P., & Grenfell, T. C. (2005). Surface Albedo of the Antarctic Sea Ice zone. *Journal of Climate*, *18*(17), 3606–3622. https://doi.org/10.1175/JCLI3489.1

Briegleb, P., Bitz, M., Hunke, C., Lipscomb, H., Holland, M., Schramm, L., & Moritz, E. (2004). Scientific description of the sea ice component in the Community Climate System Model, version 3. https://doi.org/10.5065/D6HH6H1P

Briegleb, P., & Light, B. (2007). A delta-Eddington multiple scattering parameterization for solar radiation in the sea ice component of the community climate system model. https://doi.org/10.5065/D6B27S71

Castellani, G., Losch, M., Lange, B. A., & Flores, H. (2017). Modeling Arctic sea-ice algae: Physical drivers of spatial distribution and algae phenology. *Journal of Geophysical Research: Oceans*, *122*(9), 7466–7487. https://doi.org/10.1002/2017JC012828

Clement Kinney, J., Maslowski, W., Osinski, R., Jin, M., Frants, M., Jeffery, N., & Lee, Y. J. (2020). Hidden production: On the importance of pelagic phytoplankton blooms beneath Arctic sea ice. *Journal of Geophysical Research: Oceans*, *125*(9), e2020JC016211. https://doi.org/10.1029/2020JC016211

Ehn, J. K., Mundy, C. J., Barber, D. G., Hop, H., Rossnagel, A., & Stewart, J. (2011). Impact of horizontal spreading on light propagation in melt pond covered seasonal sea ice in the Canadian Arctic. *Journal of Geophysical Research*, *116*(C9), C00G02. https://doi.org/10.1029/2010JC006908

Fichefet, T., & Morales Maqueda, M. A. (1997). Sensitivity of a global sea ice model to the treatment of ice thermodynamics and dynamics. *Journal of Geophysical Research*, *102*(C6), 12609–12646. https://doi.org/10.1029/97JC00480

Frey, K. E., Perovich, D. K., & Light, B. (2011). The spatial distribution of solar radiation under a melting Arctic sea ice cover. *Geophysical Research Letters*, *38*(22), L22501. https://doi.org/10.1029/2011GL049421

Frouin, R., & Pinker, R. T. (1995). Estimating photosynthetically Active radiation (PAR) at the Earth's surface from satellite observations. *Remote Sensing of Environment*, *51*(1), 98–107. https://doi.org/10.1016/0034-4257(94)00068-X

Gao, Y., Zhang, Y., Chai, F., Granskog, M. A., Duarte, P., & Assmy, P. (2022). An improved radiative forcing scheme for better representation of Arctic under-ice blooms. *Ocean Modelling*, *177*, 102075. https://doi.org/10.1016/j.ocemod.2022.102075

Goldenson, N., Doherty, S. J., Bitz, C. M., Holland, M. M., Light, B., & Conley, A. J. (2012). Arctic climate response to forcing from light-absorbing particles in snow and sea ice in CESM. *Atmospheric Chemistry and Physics*, *12*(17), 7903–7920. https://doi.org/10.5194/acp-12-7903-2012

Grenfell, T. C., & Maykut, G. A. (1977). The optical properties of ice and snow in the Arctic basin *. *Journal of Glaciology*, *18*(80), 445–463. https://doi.org/10.3189/S0022143000021122

Grenfell, T. C., & Perovich, D. K. (2004). Seasonal and spatial evolution of albedo in a snow-ice-land-ocean environment. *Journal of Geophysical Research*, *109*(C1), C01001. https://doi.org/10.1029/2003JC001866

Hill, V. J., Light, B., Steele, M., & Zimmerman, R. C. (2018). Light availability and phytoplankton growth beneath Arctic sea ice: Integrating observations and modeling. *Journal of Geophysical Research: Oceans*, *123*(5), 3651–3667. https://doi.org/10.1029/2017JC013617

Holm-Hansen, O., Lorenzen, C. J., Holmes, R. W., & Strickland, J. D. H. (1965). Fluorometric determination of Chlorophyll. *ICES Journal of Marine Science*, *30*(1), 3–15. https://doi.org/10.1093/icesjms/30.1.3

Horvat, C., Flocco, D., Rees Jones, D. W., Roach, L., & Golden, K. M. (2020). The effect of melt pond geometry on the distribution of solar energy under first-year sea ice. *Geophysical Research Letters*, *47*(4), e2019GL085956. https://doi.org/10.1029/2019GL085956

Horvat, C., Jones, D. R., Iams, S., Schroeder, D., Flocco, D., & Feltham, D. (2017). The frequency and extent of sub-ice phytoplankton blooms in the Arctic Ocean. *Science Advances*, *3*(3), e1601191. https://doi.org/10.1126/sciadv.1601191

Hunke, E., Allard, R., Bailey, D. A., Blain, P., Craig, A., Dupont, F., et al. (2022). CICE-Consortium/Icepack: Icepack 1.3.2. *Zenodo*. https://doi.org/10.5281/zenodo.6967671

Järvinen, O., & Leppäranta, M. (2011). Transmission of solar radiation through the snow cover on floating ice. *Journal of Glaciology*, *57*(205), 861–870. https://doi.org/10.3189/002214311798043843

Jin, Z., Ottaviani, M., & Sikand, M. (2022). Validation of a fully-coupled radiative transfer model for sea ice with albedo and transmittance measurements. *The Cryosphere Discussions*, 1–24. https://doi.org/10.5194/tc-2022-106

Joseph, J. H., Wiscombe, W. J., & Weinman, J. A. (1976). The delta-eddington approximation for radiative flux transfer. *Journal of the Atmospheric Sciences*, *33*(12), 2452–2459. https://doi.org/10.1175/1520-0469(1976)033<2452:TDEAFR>2.0.CO;2

Kari, E., Jutila, A., Friedrichs, A., Leppäranta, M., & Kratzer, S. (2020). Measurements of light transfer through drift ice and landfast ice in the northern Baltic Sea. *Oceanologia*, *62*(3), 347–363. https://doi.org/10.1016/j.oceano.2020.04.001

Katlein, C., Arndt, S., Belter, H. J., Castellani, G., & Nicolaus, M. (2019). Seasonal Evolution of light transmission distributions through Arctic sea ice. *Journal of Geophysical Research: Oceans*, *0*(0), 5418–5435. https://doi.org/10.1029/2018JC014833

Katlein, C., Arndt, S., Nicolaus, M., Perovich, D. K., Jakuba, M. V., Suman, S., et al. (2015). Influence of ice thickness and surface properties on light transmission through Arctic sea ice. *Journal of Geophysical Research: Oceans*, *120*(9), 5932–5944. https://doi.org/10.1002/2015JC010914

Katlein, C., Langelier, J.-P., Ouellet, A., Lévesque-Desrosiers, F., Hisette, Q., Lange, B. A., et al. (2021). The three-dimensional light field within sea ice ridges. *Geophysical Research Letters*, *48*(11), e2021GL093207. https://doi.org/10.1029/2021GL093207

Keen, A., Blockley, E., Bailey, D. A., Boldingh Debernard, J., Bushuk, M., Delhaye, S., et al. (2021). An inter-comparison of the mass budget of the Arctic sea ice in CMIP6 models. *The Cryosphere*, *15*(2), 951–982. https://doi.org/10.5194/tc-15-951-2021

Lecomte, O., Fichefet, T., Flocco, D., Schroeder, D., & Vancoppenolle, M. (2015). Interactions between wind-blown snow redistribution and melt ponds in a coupled ocean–sea ice model. *Ocean Modelling*, *87*, 67–80. https://doi.org/10.1016/j.ocemod.2014.12.003

Lengaigne, M., Menkes, C., Aumont, O., Gorgues, T., Bopp, L., André, J.-M., & Madec, G. (2007). Influence of the oceanic biology on the tropical Pacific climate in a coupled general circulation model. *Climate Dynamics*, *28*(5), 503–516. https://doi.org/10.1007/s00382-006-0200-2

Lewis, K. M., van Dijken, G. L., & Arrigo, K. R. (2020). Changes in phytoplankton concentration now drive increased Arctic Ocean primary production. *Science*, *369*(6500), 198–202. https://doi.org/10.1126/science.aay8380

Light, B., Eicken, H., Maykut, G. A., & Grenfell, T. C. (1998). The effect of included participates on the spectral albedo of sea ice. *Journal of Geophysical Research*, *103*(C12), 27739–27752. https://doi.org/10.1029/98JC02587

Light, B., Grenfell, T. C., & Perovich, D. K. (2008). Transmission and absorption of solar radiation by Arctic sea ice during the melt season. *Journal of Geophysical Research*, *113*(C3), C03023. https://doi.org/10.1029/2006JC003977

Light, B., Maykut, G. A., & Grenfell, T. C. (2004). A temperature-dependent, structural-optical model of first-year sea ice. *Journal of Geophysical Research*, *109*(C6), C06013. https://doi.org/10.1029/2003JC002164

Light, B., Smith, M. M., Perovich, D. K., Webster, M. A., Holland, M. M., Linhardt, F., et al. (2022). Arctic sea ice albedo: Spectral composition, spatial heterogeneity, and temporal evolution observed during the MOSAiC drift. *Elementa: Science of the Anthropocene*, *10*(1), 000103. https://doi.org/10.1525/elementa.2021.000103

Lorenzen, C. J. (1967). Determination of Chlorophyll and pheo-pigments: Spectrophotometric Equations1. *Limnology & Oceanography*, *12*(2), 343–346. https://doi.org/10.4319/lo.1967.12.2.0343

Madec, G., Bourdallé-Badie, R., Chanut, J., Clementi, E., Coward, A., Ethé, C., et al. (2022). NEMO ocean engine. https://doi.org/10.5281/zenodo.6334656

Massicotte, P., Amiraux, R., Amyot, M.-P., Archambault, P., Ardyna, M., Arnaud, L., et al. (2020). Green edge ice camp campaigns: Understanding the processes controlling the under-ice Arctic phytoplankton spring bloom. *Earth System Science Data*, *12*(1), 151–176. https://doi.org/10.5194/essd-12-151-2020

Massicotte, P., Bécu, G., Lambert-Girard, S., Leymarie, E., & Babin, M. (2018). Estimating underwater light regime under spatially heterogeneous sea ice in the Arctic. *Applied Sciences*, *8*(12), 2693. https://doi.org/10.3390/app8122693

Matthes, L. C., Mundy, C. J., L.-Girard, S., Babin, M., Verin, G., & Ehn, J. K. (2020). Spatial heterogeneity as a key variable influencing spring-summer progression in UVR and PAR transmission through Arctic Sea Ice. *Frontiers in Marine Science*, *7*. https://doi.org/10.3389/fmars.2020.00183

Maykut, G. A., & Untersteiner, N. (1971). Some results from a time-dependent thermodynamic model of sea ice. *Journal of Geophysical Research*, *76*(6), 1550–1575. https://doi.org/10.1029/JC076i006p01550

Meiners, K. M., Vancoppenolle, M., Thanassekos, S., Dieckmann, G. S., Thomas, D. N., Tison, J.-L., et al. (2012). Chlorophyll a in Antarctic sea ice from historical ice core data. *Geophysical Research Letters*, *39*(21), L21602. https://doi.org/10.1029/2012GL053478

Mobley, C. (2022). The oceanic optics book. https://doi.org/10.25607/OBP-1710

Morel, A. (1988). Optical modeling of the upper ocean in relation to its biogenous matter content (case I waters). *Journal of Geophysical Research*, *93*(C9), 10749–10768. https://doi.org/10.1029/JC093iC09p10749

Morrow, J. H., Booth, C., Lind, R. N., & Hooker, S. B. (2010). The compact-optical profiling system (C-OPS). *National Aeronautics and Space Administration Technical Memorandum*, 42–50.

Mundy, C. J., Ehn, J. K., Barber, D. G., & Michel, C. (2007). Influence of snow cover and algae on the spectral dependence of transmitted irradiance through Arctic landfast first-year sea ice. *Journal of Geophysical Research*, *112*(C3), C03007. https://doi.org/10.1029/2006JC003683

Nomura, D., Wongpan, P., Toyota, T., Tanikawa, T., Kawaguchi, Y., Ono, T., et al. (2020). Saroma-ko lagoon observations for sea ice physico-chemistry and ecosystems 2019 (SLOPE2019). *Bulletin of Glaciological Research*, *38*(0), 1–12. https://doi.org/10.5331/bgr.19R02

Notz, D., Jahn, A., Holland, M., Hunke, E., Massonnet, F., Stroeve, J., et al. (2016). The CMIP6 Sea-Ice Model Intercomparison Project (SIMIP): Understanding sea ice through climate-model simulations. *Geoscientific Model Development*, *9*(9), 3427–3446. https://doi.org/10.5194/gmd-9-3427-2016

Oziel, L., Massicotte, P., Randelhoff, A., Ferland, J., Vladoiu, A., Lacour, L., et al. (2019). Environmental factors influencing the seasonal dynamics of spring algal blooms in and beneath sea ice in western Baffin Bay. *Elementa: Science of the Anthropocene*, *7*(1), 34. https://doi.org/10.1525/elementa.372

Pedersen, C. A., Roeckner, E., Lüthje, M., & Winther, J.-G. (2009). A new sea ice albedo scheme including melt ponds for ECHAM5 general circulation model. *Journal of Geophysical Research*, *114*(D8), D08101. https://doi.org/10.1029/2008JD010440

Peixoto, J. P., & Oort, A. H. (1992). *Physics of climate*. American Institute of Physics.

Perovich, D. K. (1996). The optical properties of sea ice. *CRREL Monograph*, *96–1*, 25.

Perovich, D. K. (2007). Light reflection and transmission by a temperate snow cover. *Journal of Glaciology*, *53*(181), 201–210. https://doi.org/10.3189/172756507782202919

Perovich, D. K. (2017). Sea ice and sunlight. In *Sea ice* (pp. 110–137). John Wiley & Sons, Ltd. https://doi.org/10.1002/9781118778371.ch4

Perovich, D. K., Tucker, W. B., III., & Ligett, K. A. (2002). Aerial observations of the evolution of ice surface conditions during summer. *Journal of Geophysical Research*, *107*(C10), 8048. https://doi.org/10.1029/2000JC000449

Popova, E. E., Yool, A., Coward, A. C., Dupont, F., Deal, C., Elliott, S., et al. (2012). What controls primary production in the Arctic Ocean? Results from an intercomparison of five general circulation models with biogeochemistry. *Journal of Geophysical Research*, *117*(C8), C00D12. https://doi.org/10.1029/2011JC007112

Post, E. (2017). Implications of earlier sea ice melt for phenological cascades in arctic marine food webs. *Food Webs*, *13*, 60–66. https://doi.org/10.1016/j.fooweb.2016.11.002

Randelhoff, A., Oziel, L., Massicotte, P., Bécu, G., Galí, M., Lacour, L., et al. (2019). The evolution of light and vertical mixing across a phytoplankton ice-edge bloom. *Elementa: Science of the Anthropocene*, *7*(1), 20. https://doi.org/10.1525/elementa.357

Roach, L. A., Dörr, J., Holmes, C. R., Massonnet, F., Blockley, E. W., Notz, D., et al. (2020). Antarctic Sea Ice Area in CMIP6. *Geophysical Research Letters*, *47*(9), e2019GL086729. https://doi.org/10.1029/2019GL086729

Selz, V., Laney, S., Arnsten, A. E., Lewis, K. M., Lowry, K. E., Joy-Warren, H. L., et al. (2018). Ice algal communities in the Chukchi and Beaufort Seas in spring and early summer: Composition, distribution, and coupling with phytoplankton assemblages. *Limnology & Oceanography*, *63*(3), 1109–1133. https://doi.org/10.1002/lno.10757

Shine, K. P., & Henderson-Sellers, A. (1985). The sensitivity of a thermodynamic sea ice model to changes in surface albedo parameterization. *Journal of Geophysical Research*, *90*(D1), 2243–2250. https://doi.org/10.1029/JD090iD01p02243

SIMIP Community (2020). Arctic sea ice in CMIP6. *Geophysical Research Letters*, *47*, e2019GL086749. https://doi-org.insu.bib.cnrs.fr/10.1029/2019GL086749

Smith, R., Anning, J., Clément, P., & Cota, G. F. (1988). Abundance and production of ice algae in Resolute Passage. *Canadian Arctic*, *48*, 251–263. https://doi.org/10.3354/meps048251

Stroeve, J., Vancoppenolle, M., Veyssiere, G., Lebrun, M., Castellani, G., Babin, M., et al. (2021). A multi-sensor and modeling Approach for mapping light under Sea Ice during the ice-growth season. *Frontiers in Marine Science*, *7*, 1253. https://doi.org/10.3389/fmars.2020.592337

Vancoppenolle, M., Bopp, L., Madec, G., Dunne, J., Ilyina, T., Halloran, P. R., & Steiner, N. (2013). Future Arctic Ocean primary productivity from CMIP5 simulations: Uncertain outcome, but consistent mechanisms. *Global Biogeochemical Cycles*, *27*(3), 605–619. https://doi.org/10.1002/gbc.20055

Vancoppenolle, M., Fichefet, T., Goosse, H., Bouillon, S., Madec, G., & Maqueda, M. A. M. (2009). Simulating the mass balance and salinity of Arctic and Antarctic sea ice. 1. Model description and validation. *Ocean Modelling*, *27*(1), 33–53. https://doi.org/10.1016/j.ocemod.2008.10.005

Vancoppenolle, M., & Tedesco, L. (2017). Numerical models of sea ice biogeochemistry. In D. N. Thomas (Ed.), *Sea Ice* (pp. 492–515). John Wiley & Sons, Ltd. https://doi.org/10.1002/9781118778371.ch20

Vérin, G., Domine, F., Babin, M., Picard, G., & Arnaud, L. (2022). Metamorphism of snow on Arctic sea ice during the melt season: Impact on spectral albedo and radiative fluxes through snow. *The Cryosphere*, *16*(9), 3431–3449. https://doi.org/10.5194/tc-16-3431-2022

Veyssière, G., Castellani, G., Wilkinson, J., Karcher, M., Hayward, A., Stroeve, J. C., et al. (2022). Under-ice light field in the Western Arctic Ocean during late summer. *Frontiers of Earth Science*, *9*. https://doi.org/10.3389/feart.2021.643737

Vivier, F., Hutchings, J. K., Kawaguchi, Y., Kikuchi, T., Morison, J. H., Loureno, A., & Noguchi, T. (2016). Sea ice melt onset associated with lead opening during the spring/summer transition near the North Pole. *Journal of Geophysical ResearchOcean*, *121*(4), 2499–2522. https://doi.org/10.1002/2015JC011588

Warren, S. G. (1982). Optical properties of snow. *Reviews of Geophysics*, *20*(1), 67–89. https://doi.org/10.1029/RG020i001p00067

Warren, S. G. (2019). Optical properties of ice and snow. *Philosophical Transactions of the Royal Society A: Mathematical, Physical & Engineering Sciences*, *377*(2146), 20180161. https://doi.org/10.1098/rsta.2018.0161

Wongpan, P., Meiners, K. M., Langhorne, P. J., Heil, P., Smith, I. J., Leonard, G. H., et al. (2018). Estimation of Antarctic land-fast Sea Ice Algal biomass and snow thickness from under-ice radiance spectra in two Contrasting Areas. *Journal of Geophysical Research: Oceans*, *123*(3), 1907–1923. https://doi.org/10.1002/2017JC013711

Wongpan, P., Nomura, D., Toyota, T., Tanikawa, T., Meiners, K. M., Ishino, T., et al. (2020). Using under-ice hyperspectral transmittance to determine land-fast sea-ice algal biomass in Saroma-ko Lagoon, Hokkaido, Japan. *Annals of Glaciology*, *61*(83), 454–463. https://doi.org/10.1017/aog.2020.69

Yentsch, C. S., & Menzel, D. W. (1963). A method for the determination of phytoplankton chlorophyll and phaeophytin by fluorescence. *Deep-Sea Research and Oceanographic Abstracts*, *10*(3), 221–231. https://doi.org/10.1016/0011-7471(63)90358-9

Yu, M., Lu, P., Cheng, B., Leppäranta, M., & Li, Z. (2022). Impact of microstructure on solar radiation transfer within sea ice during summer in the Arctic: A model sensitivity study. *Frontiers in Marine Science*, *9*. https://doi.org/10.3389/fmars.2022.861994

Zhang, J., Ashjian, C., Campbell, R., Spitz, Y. H., Steele, M., & Hill, V. (2015). The influence of sea ice and snow cover and nutrient availability on the formation of massive under-ice phytoplankton blooms in the Chukchi Sea. *Deep Sea Research Part II: Topical Studies in Oceanography*, *118*, 122–135. https://doi.org/10.1016/j.dsr2.2015.02.008